Title: Cortical microtubules act as a template to organize nano-scale patterning of exocytosis

Authors: Jelmer J. Lindeboom[1,2]*, Ryan Gutierrez[1,3], Viktor Kirik[4] and David W. Ehrhardt[1,3]*

Affiliations:

[1]Department of Plant Biology, Carnegie Institution for Science; Stanford, CA 94305, USA.

[2]Current Address: Novo Nordisk Foundation Center for Genomic Mechanism of Disease, Broad Institute of MIT and Harvard, MA 02142, USA.

[3]Department of Biology, Stanford University; Stanford, CA 94305, USA.

[4]School of Biological Sciences, Illinois State University; Normal, IL 61790, USA.

*Corresponding authors

Email: ehrhardt@stanford.edu

jelmer@broadinstitute.org

Abstract

Targeting of exocytosis enables cellular morphogenesis, motility and polarized transport, yet relatively little is known about the targeting mechanisms in cellular systems. Here we show that the SEC/MUNC protein KEULE is a dynamic marker for individual secretory events and employ it as a live cell probe, that together with high-precision image analysis of thousands of events, reveal that cortical microtubule arrays act as two-dimensional templates that pattern exocytosis at the nano-scale in higher plant cells. This mechanism is distinct from previously described mechanisms involving motor-driven transport and defines ordered and adjacent linear domains where secretory events are higher and lower than expected, effectively redistributing exocytosis over most of the cell membrane. In addition, analysis of KEULE kinetics revealed distinct phases of assembly/disassembly that are differentially sensitive to experimental treatments that reduce exocytosis, revealing SEC/MUNC dynamics as a versatile and information rich read-out of exocytosis *in vivo.*

Main Text

Introduction

The ability to organize biomolecules at the cell cortex was a fundamental innovation in the evolution of cellular life, enabling essential biological functions including cellular morphogenesis, motility and polarized transport. Targeted exocytosis, non-random positioning and fusion of secretory vesicles at the plasma membrane, is a crucial mechanism for creating such cortical organization.

Across phyla, the microtubule cytoskeleton has been implicated in spatial organization of exocytosis. This functionality is exemplified in plant and fungal cells by cellular tip growth, and in animal cells by examples such as polarization of mammalian epithelia, cell migration and the positioning of focal adhesions[1,2]. The molecular polarity of microtubules plays an important role in how their function in secretory targeting is understood. For example, polarized arrays of microtubules created by nucleation from centralized organizing bodies - such as centrosomes or Golgi - can serve as directional tracks for motor-driven transport of secretory vesicles from where they are created to destinations at the plasma membrane[2,3]. This process sometimes aided by specific association of microtubule ends with the cell membrane, such as at or near targets such as focal adhesions [1]. Centrally polarized arrays of microtubules can also organize secretion through directed transport of factors that establish domains at the plasma membrane where secretion is targeted to, such as for tip growth in fission yeast[4]. However, many cells across diverse organisms feature interphase microtubule arrays that are not centrally organized and have architectures where microtubules are not clearly polarized with respect to the plasma membrane[5]. Many of these arrays are implicated in important biological functions, such as morphogenesis, but relatively little is understood about whether they act to support these functions by targeting secretion, and what the mechanisms may be.

Gaining an understanding of secretory targeting mechanisms requires the ability to observe individual secretory events with respect to targeting machineries and a means to verify successful delivery of secretory cargo. Observing individual exocytosis events has been challenging in many cell models because microtubules, secretory vesicles and the machineries of secretion are often densely concentrated. Axially growing cells in the epidermis of higher plants have features that provide an excellent experimental platform to make such observations and for investigating how acentrosomal microtubule arrays may target and pattern secretion. In contrast to cells with microtubule arrays that are polarized with respect to the cell interior and the plasma membrane, these cells feature highly ordered arrays of microtubules that lie at the cell cortex in parallel to and in contact with the plasma membrane along their lattices. Large regions of the plasma membrane lie in a single focal plane, where the individual microtubules and bundles that comprise these arrays are easily visualized due to their quasi-2-dimensional nature and comparatively low density[6]. In previous studies, we found that cellulose synthase complexes (CSCs), large integral membrane protein complexes which synthesize and extrude cellulose into the cell wall, can be used to observe individual secretory events at the plasma membrane by allowing dynamic tracking of both secretory vesicles and successfully delivered cargo in the plasma membrane[7–9]. By tracking CSCs while simultaneously imaging dynamic cortical arrays, we discovered that CSCs were preferentially delivered to the cell membrane at locations defined by microtubules. This targeting did not involve vesicular transport along microtubules, not did it involve defining secretory domains by end-on association of microtubule ends with the cell membrane[10], thus suggesting a previously undescribed mechanism for microtubule-dependent

secretory targeting. CSC's themselves have been shown to interact with microtubules via a specific linker protein (CSI1), a mechanism that can also tether CSC-containing vesicles and organelles to microtubules[11–14], so it is not clear if this secretory targeting mechanism might be unique only to delivery of CSC's to the plasma membrane.

The question of microtubule targeting of secretion is of special interest in the context of plant cell growth because ordered cortical microtubule arrays are essential to create functional cell shape. Depolymerization of microtubules by the drug oryzalin causes isotropic growth and a complete loss of genetically determined cell shape. The predominant hypothesis for the function of cortical microtubules in directing cell growth is that they guide the trajectories of CSCs as they synthesize and extrude cellulose microfibrils into the cell wall, thus creating material and mechanical anisotropy to direct expansion of the cell wall under tension by high in turgor. The hypothesis that cortical microtubules guide the trajectories of CSCs was microtubules was confirmed by live cell imaging studies[15]. However, disruption of both microtubule guidance of CSCs and CSC secretion in *csi1* null mutants causes only a modest loss of cell growth anisotropy[11,12,14]. In addition, although complete loss of growth anisotropy is caused by microtubule depolymerization, this phenotype is not due to a loss of CSC secretion[10] nor a lack of ordering in CSC trajectories[16–18], and oryzalin treated cells continue to grow at near normal rates[19]. These observations suggest that cortical microtubules arrays have additional important functions in directing cell shape, prompting us to ask if cortical microtubules may guide cellular morphogenesis by acting as a general targeting mechanism, beyond CSC's, to pattern secretion during cell growth.

To determine if secretion in growing plant cells is broadly patterned by cortical microtubule targeting, we require a dynamic biological marker that identifies single exocytotic events and is involved in a wide range of exocytotic traffic to the plasma membrane. To date, such a marker has not been identified. Imaging studies of core secretory proteins, including soluble *N*-ethylmaleimide-sensitive factor attachment protein receptors (SNARE proteins)[20–22] and components of the exocyst complex[23,24], have not revealed a clear relationship between the presence and dynamics of these proteins with verified exocytosis events nor have they shown association of these proteins with microtubules[24].

SM proteins are essential regulators of SNARE-mediated vesicle fusion. In exocytosis, SNARE proteins anchored to the vesicle interact with those on the plasma membrane and form a membrane bridging complex with other partners that enables membrane fusion[25–27]. The soluble SM proteins are known to bind to SNAREs, and evidence from genetic studies together with *in vivo* and *in vitro* experiments suggest they function in vesicle docking, SNARE complex assembly and vesicle fusion [28–33]. In plants, the *Arabidopsis* Sec1 homolog KEULE was identified in a genetic screen for embryonic pattern mutants[34], where loss of function mutations are lethal, causing bloated and multinucleate cells[35]. Consistent with other SM proteins, KEULE interacts genetically and biochemically with Qa-SNAREs, specifically KNOLLE (SYP111) and SYP121, and has been shown to play essential roles in cell plate assembly during cytokinesis and secretory traffic to the cell membrane[20,36–40]. The demonstrated function of KEULE in secretion to the plasma membrane, combined with its severe loss of function phenotype due to lack of secretion suggested that KEULE might serve as an excellent candidate for a generalized reporter of secretion.

The molecular and structural mechanisms by which SM proteins interact with and regulate SNARE complex assembly have investigated intensively by genetic, biochemical, *in*

118 *vitro* and structural studies[28–33], and SM proteins have been imaged in live cells in several
119 systems[41–48]. However, important features of their behaviors and biological function in living
120 cells remain to be uncovered. These questions include the fine scale cellular distributions of SM
121 proteins and clusters, the association of SM clusters with exocytosis events, the relationship of
122 these exocytosis events to potential organizing machineries and the dynamics of SM assembly
123 and loss at exocytosis sites, especially prior to and during vesicle fusion.

124 Here, we develop and apply automated and high precision analysis methods to detect and
125 track tens of thousands of individual fluorescently-tagged KEULE clusters to investigate their
126 dynamics and to map their positions at the plasma membrane in living cells. We evaluate these
127 clusters as secretory events by use of CSC's as a validated secretory cargo and employ genetic
128 analysis to test for the function of KEULE in CSC delivery. Finally, we employ high precision
129 mapping of KEULE clusters and microtubules, combined with Baysian statistical methods, to
130 quantitatively investigate the cortical microtubule cytoskeleton as a template in patterning
131 general exocytosis.

132

133 **Results**

134 **Functional dynamics of tdTomato-KEULE cluster formation**

135 To visualize KEULE protein *in vivo*, we created a tdTomato-KEULE fluorescent reporter
136 constructed from the chromosomal gene with native upstream regulatory sequence and
137 introduced it into *Arabidopsis* plants heterozygous for a *keule* loss of function allele. To obtain
138 plants for study of KEULE localization and dynamics, we screened for self-fertilized progeny of
139 these transgenic plants that exhibited rescue of *keule* mutant phenotype by the tagged KEULE
140 protein. These plants exhibited full rescue of plant growth and development through the 5-day
141 seedling stage used for our further studies (Fig. S1, See Methods).

142 In dark-grown *Arabidopsis* hypocotyl cells expressing the tdTomato-KEULE construct,
143 we observed KEULE signal appear as densely distributed and temporally dynamic puncta at the
144 plasma membrane (See Fig. 1A). The dynamics of signal increase and decay were apparent in
145 time-lapse movies (Movie S1), kymographs of signal intensity over time along transect lines
146 (Fig. 1B) and in sequential image samples of individual puncta (See Fig. 1C). In all, a steady
147 increase in signal intensity was observed, followed by an abrupt decrease and disappearance of
148 signal. This behavior indicates the accumulation and loss of many fluorescently labeled KEULE
149 proteins, which we will refer to hereafter as clusters.

150 The dynamics of tdTomato-KEULE accumulation and disappearance are presumably
151 related to its function. Therefore, we reasoned that a quantitative and robust picture of KEULE
152 cluster dynamics would be useful in gaining insight into the underlying molecular mechanisms
153 of secretion. To accomplish this, we collected a large-scale and high-resolution dataset
154 comprising thousands of individual events. We acquired streamed images at 200 ms intervals and
155 performed automated detection and frame-to-frame linking of KEULE cluster signal using
156 µTrack[49]. This track information was then used to extract position and intensity information by
157 Maximum Likelihood Estimate 2D Gaussian fitting[50] (for details see Methods, Movie S2). To
158 define events of signal appearance, accumulation and loss, we used a minimum sample of 4
159 sequential acquisitions, which made our shortest measured lifetimes approximately 800 ms. The
160 lifetime distribution of tdTomato-KEULE clusters showed a large range, from this minimal event

length of 800 ms to over half a minute. The data followed a roughly exponential distribution with a mean of 2.34 s and ~95% of lifetimes being less than 7 seconds long (See Fig. 1D).

The large lifetime range of observed KEULE cluster events might represent a collection of functional classes. If so, such classes may by differentiated by their kinetics. To assess the kinetics KEULE signal accumulation and loss, and to ask if these kinetics might vary as a function of cluster lifetime, we leveraged our large data set to calculate KEULE kinetics for each 200 ms lifetime increment. Fig. 1E shows average intensities for all observed clusters with lifetimes of 4.2, 4.4 and 4.6 s. All these plots show a similar pattern: an initial steep rise in intensity, followed by a steady increase, then a short plateau phase, and ending with a sharp decrease. When we extended this analysis over a larger range of lifetimes, we observed evidence that the shorter-lived events accumulated tdTomato-KEULE intensity at a slower rate, suggesting they might be a functionally different class (See Fig. 1F). At longer lifetimes, the plateau phase became more extended, suggesting that these events may be paused or stalled (See Fig. 1F). To examine further these differences in accumulation kinetics as a function of cluster lifetime, we grouped events into three classes; short (0.8 to 1.6s), medium (1.8 to 6.2s) and long (6.4+s) – and then averaged the intensities at each 200 msec timepoint (Fig. 1G, for details see Methods). The timepoints following the plateau phase were omitted to reveal better differences or similarities in signal accumulation. This analysis confirmed that, indeed, the short events show significantly slower signal accumulation (See Fig. 1G). Interestingly, the medium and long tdTomato-KEULE cluster lifetimes show nearly identical trends in signal intensity accumulation over time, indicating that they might be part of the same functional population during KEULE recruitment/assembly. It is noteworthy that for events up to ~5s, longer-lasting events reach a higher maximum cluster signal intensity. A possible explanation for this phenomenon is that larger vesicles require a larger area for membrane fusion and therefore more KEULE. Unlike the medium class, the long class exhibited a prolonged plateau phase, possibly indicating stalled exocytosis events or alternatively, an extended checkpoint for a class of exocytosis events involving a large amount of KEULE, and therefore perhaps larger secretory vesicles.

Clusters of tdTomato-KEULE coincide with CSC delivery to the plasma membrane

To place SM protein accumulation in context of functional exocytosis, we took advantage of our previous work on delivery of CSCs to the plasma membrane[7]. CSCs are assembled in the Golgi system from multiple CESA catalytic subunits[51,52], move through the trans-Golgi network (TGN) and are budded off into secretory vesicles that fuse with the plasma membrane[7]. Because CSCs are formed of multiple CESA subunits, they can be labeled by fluorescent proteins in sufficient number to allow their detection and the tracking of individual complexes during the process of exocytosis. Labeled vesicles display rapid and erratic dynamics that abruptly become stabilized at the optical plane of the plasma membrane with a mean duration of about 60 seconds, followed by a transition to slow, steady and typically linear motility of between 250 and 450 nm/min. The transition erratic to static movement is interpreted as evidence for vesicular capture and tethering at the plasma membrane, and the transition to slow and steady movement indicates successful vesicle fusion and delivery of CSCs, which are propelled by the synthesis and extrusion of cellulose microfibrils[15,17]. This stereotyped behavior makes CSCs an excellent reporter for successful exocytosis, revealing a time and place for vesicle tethering, and distinguishing vesicle tethering at the plasma membrane from successful vesicle fusion and cargo delivery.

To visualize KEULE together with CSCs, we generated plants that express tdTomato-KEULE and CIT-CESA6, a catalytic CSC subunit labeled with Citrine fluorescent protein[53] in a *keule*/*cesa6* double mutant background (See Methods). CIT-CESA6 signal is relatively dense in the plasma membrane of rapidly growing cells so we photobleached the CIT-CESA6 signal over a region of the plasma membrane to aid detection of new CSC arrivals and their relation to td-Tomato-KEULE signal (See Fig. 2A, Movie S3). For each CSC arrival at the optical plane of the plasma membrane, we determined the first frame in which the CESA6 signal became stationary (an indication of interaction and tethering at the plasma membrane). We then identified the nearest KEULE cluster in a range of -10 to 50 seconds of the first stable CESA6 frame and determined the distance between the centroid of the CESA6 signal and the centroid of the nearest KEULE signal by maximum likelihood 2D Gaussian fitting (See Methods). A search range starting at -10 seconds was chosen because the exact frame of stationary transitions was in some cases obscured by signal from clusters of other labeled organelles such as Golgi bodies and TGN. If KEULE is involved in the exocytotic delivery of CSCs to the plasma membrane, we expect to observe co-localization between CSC delivery events and KEULE clusters. However, CSC deliveries, as defined by static tracks, are relatively sparse and long lived as compared to KEULE cluster events, so some degree of colocalization in space and time is expected by chance alone. To assess statistically the spatial and temporal association of CSCs delivery events and KEULE clusters, we generated a simulated dataset of random locations within the photobleaching areas and identified the nearest KEULE spot to those random spots within the same time window we used for our experimental observations. We then compared the distribution of distances to the nearest KEULE cluster between the CSC deliveries and simulated spots (See Fig. 2B and D) and found that the experimental data were strongly skewed to shorter distances ($p < 3.4$ e-56, Mann-Whitney U test). The pattern of over- and under-representation of observed with respect to simulated data is more easily seen in a plot of the bin-by bin differences where shorter KEULE to microtubule distances are over-represented and longer distances are underrepresented (See Fig. 2C). Using a Bayesian method (See Methods), we show that the most likely value of the experimental bias from the null hypothesis of a random association is significantly above that expected by chance alone for CSCs with distances < 200 nm (See Fig 2E and F) and longer distances are significantly (and strikingly) underrepresented in the experimental data. Based on these data we define colocalization as observing a KEULE cluster centroid within 200 nm from the position of CSC signal in the first frame in which it was observed to stabilize (and in a time window of -10 to 50 seconds around that frame). By these criteria, we found colocalization in 81% (157 out of 194) of observed delivery events compared to 29% (13035 out of 45051) of random locations at the plasma membrane ($p < 1.4$e-50, Fisher's exact test).

We considered that our automated experimental protocol may allow for underestimation of colocalization between CSC delivery and KEULE. For example, the time interval used for these experiments is 2.11 s, of which 400 ms is used for KEULE illumination. Since a substantial portion of KEULE spot lifetimes at the plasma membrane is shorter than the ~1.7 s gap in each acquisition cycle when KEULE is not illuminated, we do not expect to detect all KEULE spots within the -10 to 50 second experimental window. In addition, not all illuminated KEULE foci are successfully detected by the detection and filtering routines used for large-scale data collection. To understand how these two cases, no illumination and no detection, affect our colocalization results, we performed a hand-curated analysis using a custom MATLAB GUI. For each CSC delivery, we examined whether there was overlap of KEULE signal with the centroid

252 of the CSC signal in the first stable frame (tethering frame). We found that in 92% (159 out of
253 172) of the cases, KEULE signal was overlapping with the position of CSC in the tethering
254 frame within -10 to 50 s of CSC stabilization, suggesting that our automated analysis may indeed
255 underestimate the true degree of colocalization frequency of CSC exocytosis events and KEULE.

256 The durations of KEULE clusters associated with CES deliveries had a distribution
257 similar in character to that observed For KEULE clusters in general (Fig. 3A, compare to
258 Fig.1D), with both appearing roughly exponential but long tailed. While lifetimes of clusters
259 associated with CESA deliveries spanned a similar range of durations, those associated with
260 CESA delivery were observed to have a significant bias towards longer values, with clusters
261 associated with CESA having a median duration of 4.3 seconds, as compared to 2.3 seconds for
262 clusters in general. To test the significant of this observed bias, we compared the proportions of
263 durations longer than two seconds and found a highly significant difference - 59% vs 37% for
264 CESA delivery-associated KEULE clusters events vs clusters in general (p=6.07E-09, Fisher's
265 exact test). These results indicate that KEULE clusters with a wide range of lifetimes are
266 associated with verified exocytosis events, with those associated with CESA complexes, which is
267 a relatively large complex, biased towards longer lifetimes.

268 If KEULE has a function in CSC exocytosis, we also expect that KEULE clusters both
269 are colocalized with CSC static phases and that the time between the start of the static CSC
270 phase and the first detected KEULE spot has a non-random distribution. Indeed, the time offset
271 between stable CSC and nearest KEULE spot observed is non-random and significantly differs
272 from the random distribution of the simulated data ($p < 7.8e-04$ Mann-Whitney U test) (See Fig.
273 3B). These data show that the appearance of the nearest KEULE cluster correlates in time with
274 the CSC signal becoming stabilized at the plasma membrane with a median time delay of 2.111 s
275 (mean = 7.92 s), suggesting that KEULE is typically recruited and functions within several
276 seconds after the time the CSC vesicle becomes stationary, and is presumably tethered, at the
277 plasma membrane. These data now provide insight into the kinetics of SM protein recruitment
278 and vesicle fusion relative to secretory vesicle stabilization and tethering at the plant cell
279 membrane.

280 KEULE abundance is significantly increased at confirmed sites of CSC exocytosis in
281 both space and time, but is it required for CSC exocytosis? To answer this question, we
282 quantified CSC delivery in seedlings of parental plants expressing CIT-CESA6 and segregating a
283 tdTomato-KEULE allele in a background homozygous for both *cesa6* and *keule* loss of function
284 (See Methods). Seedlings examined for loss of KEULE function were identified by
285 morphological *keule* phenotype and little to no tdTomato-KEULE signal. We found that the CSC
286 delivery rate was reduced by over 17-fold, which is a significant ($p<0.0001$, Wilcoxon two
287 sample test) and quantitatively substantial reduction (See Fig. 2G). The seedlings that showed
288 little to no tdTomato-KEULE fluorescence were severely reduced in size, showed large,
289 misshaped cells and did not grow beyond the size of a 2-day old wild type seedling. Taken
290 together our results indicate that KEULE plays an essential role in exocytosis of primary CSCs,
291 and that CSC secretion is spatially and temporally associated with KEULE clusters, which have
292 stereotyped dynamics of assembly and loss.

293

294 **KEULE cluster dynamics are sensitive to perturbations that reduce exocytosis**

295 We previously reported that the number of active CSCs in the plasma membrane were
296 rapidly and significantly reduced by treatment with mannitol (osmotic stress) and the herbicide
297 isoxaben[7]. Measurements of CSC delivery revealed that mannitol treatment also caused a 100-
298 fold reduction in the delivery rate of CSC's, indicating that CSC loss at the cell membrane was
299 likely caused primarily by inhibition of secretion. Isoxaben has been characterized as a specific
300 cellulose synthase complex inhibitor[54], but its mode of action is not well understood. Here we (1)
301 determine if isoxaben treatment also reduces CSC exocytosis and (2) ask if analysis of KEULE
302 dynamics may provide insight into how these treatments act to inhibit exocytosis.

303 To address the questions above, we imaged cells expressing tdTomato-KEULE and Cit-
304 CESA6 following treatment with mannitol, isoxaben or carrier only (mock). We assayed CSC
305 delivery to the plasma membrane as described above and found that, like mannitol, isoxaben is
306 also a potent inhibitor of CSC secretion (Fig. S2).

307 Following mannitol and isoxaben treatment tdTomato-KEULE cluster intensity
308 dynamics overall displayed a similar signature as observed in mock treatment - a steady increase
309 in signal and a plateau phase followed by an abrupt disappearance of signal (See Fig. S3 A).
310 These results suggest that mannitol and isoxaben treatment do not inhibit exocytosis of CSCs in
311 a manner that absolutely blocks KEULE accumulation. However, when comparing accumulation
312 dynamics grouped for short, intermediate and long events, we see striking differences among
313 treatments (See Fig. S3B). Both short- (0.8-1.6s) and intermediate-lived (1.8-6.2s) events in the
314 mannitol treated cells accumulated tdTomato-KEULE signal more slowly and to lower levels
315 than in the mock treated cells. Intriguingly, the dynamics for tdTomato-KEULE clusters that last
316 for 6.4 s or more exhibited a markedly different pattern. Initially, from 0 to ~6 s, signal
317 accumulation was indistinguishable between mannitol and mock treated cells. After ~6 s,
318 intensity gain was stalled in mock treated cells but continued to steadily increase in those treated
319 with mannitol. Taken together, these data suggest that mannitol application, and the osmotic
320 stress it causes, has bimodal effects on KEULE dynamics and may impact exocytosis by more
321 than one mechanism. By contrast, we observed that isoxaben treatment slowed accumulation of
322 tdTomato-KEULE across events of all durations (Fig. S3 C).

323 We observed related differences among treatments in KEULE cluster lifetimes. In comparing the
324 distributions of cluster lifetimes in mock and mannitol treated cells, a bimodal effect was again
325 observed, with both shorter and longer lifetimes being over-represented in comparison with
326 mock treatment (and intermediate events being under-represented) (Fig S4A, B, D). As was the
327 case with intensity dynamics, isoxoben treatment showed more of a unimodal effect, with the
328 lifetime distribution being shifted to the left (Fig. S4B, C, E). Mannitol and isoxaben also caused
329 diverging effects on persistence of KEULE clusters, as assessed by survival analysis (Fig.
330 S4F,G). Interestingly, the rates of new KEULE cluster formation under both treatments were
331 similar to that observed in the mock control (Fig. S4H), indicating that initiation of cluster
332 formation was not affected. Taken all together, our data show that KEULE cluster dynamics are
333 sensitive to perturbations that affect exocytosis and reveal evidence that mannitol and isoxoben
334 treatments affect these dynamics in distinct ways, suggesting that may act on different aspects of
335 exocytosis.

336

337 **Microtubules define spatial patterns of exocytosis**

338 In this study we showed that exocytosis of cellulose synthase complexes (CSCs) is
339 marked by formation of KEULE clusters (Fig. 2) and we measured the mean flux of CSC
340 deliveries as 1.59 events per μm^2 per h (Fig. 2G). However, the mean flux of KEULE cluster
341 formation was 134.4 events per μm^2 per h (Fig. S4H), or 85-fold higher. Therefore, CSC
342 delivery only accounts for a small fraction of the KEULE foci at the plasma membrane. Here, we
343 utilize KEULE clusters as a more generalized marker for secretion to ask if microtubules pattern
344 CSC secretion specifically or if microtubule positioning of secretory machineries is a broader
345 and fundamental function for the interphase microtubule cytoskeleton. It is important to point out
346 that another possibility is that cortical microtubules might in fact interfere sterically with many
347 secretory events, yielding an overall antagonistic relationship. To differentiate between these
348 alternatives, we performed a large-scale quantitative analysis of the positions of KEULE events
349 relative to the locations of cortical microtubules.

350 To visualize KEULE cluster events together with cortical microtubules, we performed
351 live cell imaging at 1 second intervals in hypocotyl cells of *Arabidopsis* seedlings expressing
352 GFP-TUA5 and tdTomato-KEULE in a *keule* knock-out background (See Fig. 4A, Movie S4).
353 After tracking individual KEULE events at the plasma membrane and using MLEwG fitting to
354 extract positional information (Fig. 4B, See Methods), we identified the frame with peak
355 tdTomato-KEULE intensity as the reference point for each detected KEULE cluster position
356 (Fig. 4C panels 1-3). We then measured signal intensity in the microtubule channel along a series
357 of scan lines that were rotated at 9° intervals around the centroid of the KEULE cluster (See
358 Methods and Fig. 4C panel 4). On each of these scan lines, we detected all microtubule signal
359 peaks and fit them with a modified quasi-1-dimensional MLEwG fit (See Methods, Fig. 4D).
360 Since the microtubule signal is best represented as a quasi-1-dimenional Gaussian orthogonal to
361 the microtubule axis, we determined the orientation of the nearest microtubule as identified by
362 peak analysis and used the scan line most orthogonal to the microtubule angle for determining
363 the location of the microtubule central axis closest to the KEULE spot in question (Fig. 4C, panel
364 5). For the example, for the most orthogonal scan line shown in Fig. 4C panel 5, the intensity of
365 KEULE signal in photoelectrons is shown in Fig. 4D panel 1, the triple Gaussian MLEw1dG fit
366 in panel 2, and the decomposed individual peak fits in panel 3. We used the fit positional
367 coordinates of the nearest microtubule signal peak and the KEULE cluster to calculate the
368 distance and the photoelectron fit values to estimate the standard error of the measurement (See
369 Methods and Fig. 4C panel 6). We repeated this process for all detected KEULE tracks in each
370 movie to assess the spatial relationship between KEULE clusters and the nearest microtubules to
371 those clusters (Fig. 4E, panel 1).

372 To ask if the measured distribution of KEULE to microtubule distances differs from that
373 expected if KEULE cluster positions are independent of microtubule locations (the null
374 hypothesis), we first needed to determine what the expected distributions are under the null
375 hypothesis using our detection and analysis routines within the regions of interest in which we
376 made our experimental observations. For example, microtubule array structure, which varies
377 within and among cells, will have a strong influence on this distribution, as will the dimensions
378 of our detection kernels. Therefore, we generated a simulated set of random locations within
379 each region of interest across the length of the movies and calculated the distances from these
380 synthetic KEULE foci to the nearest microtubule (Fig. 4E, panel 2). This allows us to compare
381 the distribution of experimentally observed data to that expected if KEULE cluster positions are
382 independent of microtubule locations. If KEULE cluster positions are distributed at random with
383 respect to microtubule array structure, these two distributions should converge on identity at

large sample sizes. When the experimental and expected distributions are plotted together as relative frequencies, they show evidence for distinct differences (Fig. 5A and B). To quantify over- or under-representation of the experimental data given the expected data under the null hypotheses, we used a Bayesian method to determine the most likely positive or negative bias at each distance bin (See Fig. 5C and D and Methods). We found that at KEULE-microtubule distances smaller than 180 nm, the maximum likelihood bias was significantly positive (more frequent than expected) and between 180 and 700 nm this bias was significantly negative (less frequent than expected). At distances > 700 nm we again found a positive, but smaller, bias (Fig. 5D). This spatial pattern of under- and over-representation is more easily visualized in a plot of the differences between observed and expected frequencies (Fig. 5B).

When examining patterns of KEULE foci, we also observed that sites of previous exocytosis events were 3.4 times more likely to show consecutive exocytosis events than random sites at the plasma membrane (Fig. S5). Such "hot spots" were also significantly over-represented within 180 nm of microtubules, but only modestly so (1.25 times more likely) (Fig. S5F).

Taken together, our results reveal that microtubules spatially organize exocytosis machinery by increasing the frequency of KEULE cluster formation within about 180 nm of the center of the microtubules, a distance about 7 times the dimension of a single microtubule, while at the same time decreasing the probability of KEULE cluster formation distally over a region that is about 3 times as wide. This acts effectively as a concentrating mechanism for KEULE cluster events that is patterned by cortical microtubule organization. As these KEULE clusters overlap heavily in their dynamic characteristics with those observed associated with validated exocytosis events of CSCs, this is strong evidence that microtubule organization of secretion is not confined to guiding insertion of CSCs but is a more generalized feature of secretion in growing plant cells.

Discussion

To assess imaging of SM/KEULE clusters as a general marker for exocytosis it was important to answer two questions; if there are different types of signal foci that may represent multiple types of cellular structures or functional events, and what features of signal dynamics are associated with exocytotic events. For example, some exocytotic proteins, including V-SNARES and constituents of the exocyst, have been shown to arrive at the site of exocytosis on exocytotic vesicles themselves, while others reside in the cytosol or associate with the plasma membrane and are recruited to the exocytosis site. While we found some evidence for KEULE signal on cytosolic organelles, these foci were relatively infrequent and were easily identified by their positional dynamics. Further, in experiments using labeled CSCs as a trackable secretory cargo, no KEULE signal was detected arriving at validated secretory sites on CSC containing vesicles, indicating that KEULE clusters at the cell membrane form by recruitment of KEULE to sites of secretion after arrival and interaction of cargo-carrying organelles with the plasma membrane. KEULE assembly dynamics of clusters associated with CSC secretion had similar characteristics as the KEULE population in general, including a wide range of cluster lifetimes from a couple of seconds to half a minute and stereotyped dynamics of signal accumulation and loss. The demonstrated functions of SM proteins in mediating SNARE complex formation and membrane fusion, together with their stereotyped dynamics and tight association with CSC secretion, indicate that dynamic KEULE clusters are valuable markers of individual secretory events.

429 Our measurements of thousands of KEULE clusters at the plasma allowed us to analyze
430 patterns of signal accumulation and loss as a function of varying cluster duration - revealing
431 features of, and raising new questions about, the underlying mechanisms of secretory machinery
432 assembly, maturation and resolution. Over all durations, KEULE recruitment features an initial a
433 phase of rapid accumulation, followed by continued recruitment at a slower rate. This pattern
434 suggests two phases of recruitment with different kinetics. The second rising phase is near linear,
435 indicating a near constant rate of addition over time, characteristic of mechanism such as
436 polymerization, rather than recruitment of SM proteins to a fixed number of pre-existing binding
437 sites. Such a kinetic might be consistent with the sequential addition of SM-bound SNARE-PINs
438 to a growing chain of laterally-interacting SNARE-PINs at the vesicle-plasma membrane
439 interface[55–57]. This accumulation phase ends and transitions to a plateau, after which signal
440 abruptly decays to non-detectible levels. Both the final signal level and the length of the pause
441 state correlate positively with cluster assembly time, with longer assembly times having higher
442 signal levels and longer pause durations. Over the population of observed events, global peak
443 signal is reached at durations of about 6 seconds, after which longer events involve no further
444 signal accumulation but feature only lengthened plateau times. The plateau phase could represent
445 a state where all the SNARE complexes required have been recruited to the fusion site and the
446 components of the fusion super complex are transitioning to a functionally competent state prior
447 to the enactment of membrane fusion. The plateau could also reflect an assembly checkpoint.
448 Previous *in vitro* studies have found that greater numbers of SNARE proteins are recruited to
449 interfaces of large vesicles and planar membranes[58,59]. It is possible, therefore, that our
450 measurements of KEULE dynamics are shaped in part by a distribution of vesicle sizes, with
451 longer assembly phases that build a brighter SM signal representing assembly of secretory
452 machinery at larger vesicles.

453 We found that KEULE dynamics were changed when we disrupted exocytosis with
454 osmotic stress by treatment with mannitol, or by application of a drug, isoxaben. The changes in
455 dynamics were qualitatively different for the two antagonists, indicating that they likely act on
456 different processes affecting secretion. These observations indicate that KEULE dynamics,
457 which indicate functional aspects of vesicle fusion, are a sensitive and useful readout, or marker,
458 for studying exocytosis and agents that disrupt or alter exocytosis.

459 High resolution mapping and Baysian statistical analysis of individual secretory events
460 marked by KEULE clusters revealed that these events are not randomly distributed in growing
461 hypocotyl cells but are significantly over-represented in domains defined by the cortical
462 microtubule array. This patterning of secretion differs from previously described mechanisms for
463 secretory targeting by microtubules. In the latter, the positioning of microtubule plus ends define
464 the locations for motor-transported delivery of either the secretory vesicles themselves or
465 proteins that act in defining secretory domains. By contrast, our data indicate that every part of
466 the microtubule is associated with secretory targeting, making the entire cortical array a dynamic
467 and steerable template for secretory patterning and organization of the cell cortex (Fig, 6A).

468 High precision measurement of both microtubule and KEULE cluster locations revealed
469 that the spatial range of influence for microtubule secretory targeting is significantly larger than
470 the scale of microtubules themselves. These measurements revealed that domains of higher
471 secretion frequency are approximately 180 nm wide on either side of the center of microtubules
472 or microtubule bundles, creating ~360 nm wide liner domains on average. Our analysis also
473 revealed adjacent domains, from approximately 180-700 nm from microtubule centers, where

474 KEULE cluster density was lower than expected by chance alone (Fig. 5). These results indicate
475 microtubule pattern secretion both positively and negatively and do so over spatial domains
476 larger than a micron wide, whereas the scale of microtubules are ~25 nm and bundles of two
477 microtubules in the range of 75 nm wide [60]. The width of the combined over-represented and
478 under-represented domains are about half the mean distance between ordered microtubules and
479 microtubules bundles in these cells [61], suggesting that secretion in most of the observed plasma
480 membrane is influenced by microtubules in these cells (Fig. 6B). In addition, the combination of
481 wider depleted domains coupled with narrower domains of elevated KEULE cluster density
482 suggests a concentrating effect that further enhances the relative difference in secretory
483 trafficking adjacent to microtubules as compared to distances several hundred nanometers away.

484 One mechanism that could explain the spatial scales of these microtubule-associated
485 secretory domains is direct interaction of secretory organelles with cortical microtubules, such as
486 we previously observed for vesicles containing CSC's[7,62]. Microtubule-tethered secretory
487 vesicles might capture local KEULE associated with the cell membrane, perhaps as bound to
488 SNARE partners such as SYP121[36], depleting KEULE concentration in the nearby plasma
489 membrane and making secretion there less likely, thus creating the observed zones of reduced
490 secretion (Fig. 6B). Alternatively, upstream exocytotic machinery, such as plasma-membrane
491 associated components of the exocyst complex, might be recruited by a microtubule-organized
492 membrane domain, elevating location concentration while causing depletion and thus vesicle
493 capture at a distance (Fig. 6B). Evidence that such microtubule-organized membrane domains
494 might exist has been suggested by observations of the plasma membrane associated actin
495 polymerase Formin1, which reveals narrow "dark" linear domains defined by cortical
496 microtubules where fluorescently-tagged Formin1 is excluded[63].

497 The observed flux of KEULE clusters per unit area and time was about 85-fold higher than that
498 measured for CSC delivery, therefore far more exocytosis events are associated with domains
499 defined by microtubules than can be accounted for by CSC secretion alone, implying either that
500 many or most exocytosis events in these cells are influenced by microtubules to some degree, or
501 that a quantitatively significant subpopulation of specialized traffic is redistributed, ~13% of
502 KEULE clusters as measured by our analysis. One possibility for specialized secretory traffic
503 targeted by cortical microtubules are cargoes involved in cell wall biosynthesis and cell wall
504 expansion. Supporting this idea is that KEULE has been shown to be an essential partner of the
505 Qa-SNARE SYP121, which is implicated by a growing body of evidence in mediating secretion
506 required for cell growth and expansion[21,36,37,64,65]. Cellulose is synthesized at the plasma
507 membrane, while many other structural oligosaccharides, such as pectins[66], and wall-active
508 proteins, such as expansins[67], are secreted. Targeting this secretory traffic by cortical
509 microtubule arrays to the same locations where newly synthesized cellulose microfibrils are also
510 being laid down could help coordinate the assembly of these diverse components to build a
511 functional cell wall. In addition to coordination of wall assembly, it is possible that the patterned
512 delivery of cell wall oligosaccharides and cell wall active proteins could itself act to support the
513 anisotropic expansion of cell walls required to create specific cell shape. Targeting the delivery
514 of proteins and other molecules that promote wall remodeling by ordered microtubule arrays
515 could create linear and parallel microdomains of increased wall extendibility that lie
516 perpendicular to the main axis of the cell growth - shaping the anisotropy of cell wall expansion
517 in the same direction as proposed in prevailing models for constraint of expansion by cellulose
518 microfibrils organized by microtubules[68]. As discussed in the introduction of this manuscript, an
519 important reason to consider alternative functions for cortical microtubules arrays in guiding cell

wall expansion and cell shape is that experimental evidence suggests that guidance of cellulose deposition and CSC secretion alone is not sufficient to explain the anisotropy of cell wall expansion and cell growth. Microtubule targeting of wall-active secretion could also help explain redirection of cell growth in response to signals, such as blue-light stimulation of phototrophic growth. Perception of blue light by Phototropin receptors causes a rapid 90° reorientation of cortical microtubule arrays[69], but the following redirection of expansion cannot be easily explained by directed cellulose deposition model since previously synthesized cellulose is deposited perpendicular to the direction of expansion. Microtubule targeting and patterning of wall-active secretion might allow for redirection of cell expansion regardless of cellulose orientation.

The insights we gained into patterning of secretion by cortical microtubule arrays was enabled by having an experimental platform and methods that made measuring and assessing many thousands of discreet molecular events possible. A secretory protein, such as KEULE, that is implicated in mediating a wide range of a cell's secretory traffic might be expected to be subject to a range of targeting mechanisms, including no targeting at all. Such a background can easily obscure a meaningful association between the secretory marker and a hypothesized secretory machinery. Very large sample sizes and appropriate methods to test for meaningful associations, such as we employed here, can robustly reveal such otherwise hidden relationships.

The fact that growing plant cells have a planar microtubule array that is associated with the cell membrane, and that exocytotic events as marked by KEULE protein are of relatively low density, has provided an excellent platform to study how microtubules pattern exocytosis, and do so at the level of individual exocytotic events. When we consider cellular microtubule function in cellular trafficking, we typically think of directed transport of cargos by kinesins and dynein. In contrast, this work highlights that microtubules can also function as scaffolds for organizing exocytosis. This scaffolding function for microtubules might be considered in other systems where there is indirect evidence that microtubules regulate exocytosis where they interact with the plasma membrane, such as in focal adhesions and neuronal growth cones[1,70,71]. In addition, scaffolded guidance of secretion should also be considered in the context of disease. For example, amyotrophic lateral sclerosis (ALS) risk is associated with genetic variants which reduce levels of functional UNC13A[72,73], and with genetic variation within several microtubule associated proteins[72–75]. It is possible that these proteins all converge on the same biological process of microtubule dependent patterning of exocytosis.

552 **Materials and Methods**

553 Generation of transgenic lines

554 The *pKEULE-tdTomato-KEULE* construct was generated by modifying the Gateway-
555 compatible vector pMDC43[76]. A 2049-bp region immediately upstream of the start codon of
556 *KEULE* (At1g12360) was amplified with primers
557 CGTTTAAACTACAGTTCCATTGGAGCAAC and TAGGTACCTGCGATCTAACAATTT
558 CAGACTTC. The tdTomato gene was amplified from a donor vector[77] with primers
559 CAGGTACCATGGTGAGCAAGGGCGAGGAGGT and TGGCGCGCCCTT
560 GTACAGCTCCTCCATGCCGT. The 35S promoter of pMDC43 was exchanged with the
561 *KEULE* upstream regulatory region via PmeI and Acc65I sites, and GFP in pMDC43 was
562 exchanged with *tdTomato* via KpnI and AscI sites. The full-length *KEULE* gene was amplified
563 from genomic DNA using primers GGGGACAAGTTTGTACAAAAAAGCAG
564 GCTTGACCATGTCGTACTCTGACTCC and GGGGACCACTTTGTACAAGAAAGCTGGG
565 TTTATTTGGAGATCGTCTA and then inserted into the modified pMDC43 vector using
566 Gateway cloning technology (Invitrogen) as described previously[78]. The construct was
567 introduced into plants heterozygous for the keulemm125 deletion mutation[79] via Agrobacterium-
568 mediated transformation[80,81]. T2 plants were genotyped for the *KEULE* locus using PCR: primers
569 CGACCTTATCAGAGAGCAAGG and Keu-as0 (ACAGGGATTTGATTTGAGATCTGG)
570 amplified a 1661-bp fragment from the wild-type allele and a 1505-bp allele from the deletion
571 allele. Additionally, the primer pair GTCTGTTAACGGCTGCAGAA and Keu-as0 was used to
572 amplify a fragment (1103 bp) only present in the wild-type allele. A T2 plant homozygous for
573 the deletion allele and hemizygous for the *pKEULE-tdTomato-KEULE* transgene was isolated.
574 A doubly homozygous line was subsequently isolated in the T3 generation and used for
575 experiments.

576 To generate double-labeled plants expressing markers for KEULE protein and cellulose
577 synthase, homozygous *pKEULE-tdTomato-KEULE/ keulemm125* plants (ecotype Landsberg)
578 were crossed with homozygous *pCESA6-Citrine-CESA6/cesa6prc1-1* plants (ecotype
579 Columbia[53]. An F2 line was selected that was homozygous for both mutations and hemizygous
580 for both markers. In the F3 generation, a quadruply homozygous plant was isolated together
581 with a plant homozygous for both mutations, homozygous for *pCESA6-Citrine-CESA6* and
582 hemizygous for *pKEULE-tdTomato-KEULE*. Seed from the latter plant thus show segregation
583 for the *keule* mutant phenotype.

584 To generate double-labeled plants expressing markers for KEULE protein and
585 microtubules, *p35S-EGFP-TUA5* was introduced into *pKEULE-tdTomato-KEULE/keulemm125*
586 plants via Agrobacterium-mediated transformation. T2 seedlings expressing the microtubule
587 label were used for experiments.

588

589 Growth

590 Seedlings were grown in the dark on vertical agar plates as described in Lindeboom et al.[69].
591 For hypocotyl elongation assays, seedlings were grown for 5 days. For live cell imaging
592 experiments, seedlings were imaged 3 days after germination.

593

594 Drug treatments

595 Oryzalin, taxol and isoxaben were dissolved in DMSO for 100x stock solutions. Oryzalin
596 was used at a final concentration of 20 µM, taxol (Sigma) at 20 µM and isoxaben (Sigma) at 100
597 nM in plant growth media (Hoagland's No. 2). Mannitol was dissolved in plant growth media

598 directly at a concentration of 200 mM. For control treatment (mock), DMSO was added to the
599 growth media to a final concentration of 0.01%. Incubation of the seedlings was performed in 6-
600 well plates (WVR, nontreated) with 2 mL of plant growth media in each well. The plates were
601 wrapped in aluminum foil to block light and incubated at 22 °C. The drug treatment durations
602 were 16 hours for oryzalin, and 2 hours for all other treatments. Likewise, the mock treatments
603 were 16 hours for comparison to oryzalin, and 2 hours for comparison to the remaining
604 treatments.
605
606 Confocal microscopy
607 Imaging was performed on an instrument featuring a CSU-X1 spinning disk head
608 (Yokogawa Electric), a DMI6000 B inverted microscope (Leica), a 100X/1.4 NA oil immersion
609 objective (Leica), an Evolve 512 EMCCD camera (Photometrics) and a 1.2X telescope between
610 the spinning disk unit and camera. EGFP/CITRINE and tdTomato were excited at 488 nm and
611 561 nm respectively, by solid-state lasers (Coherent Cube). Switching, shuttering and intensity of
612 these lasers was performed by direct electronic control. Emission filtering was accomplished
613 with bandpass filters, (525/50 nm for EGFP and CITRINE and 636/37 nm for tdTomato
614 (SemRock), together with a 405/488/568 nm dichroic filter (SemRock). Exposure times were
615 400 ms for tdTomato-KEULE, 200 ms for EGFP-TUA5 and 800 ms for Citrine-CESA6. Images
616 were acquired at 1 second intervals in experiments in which both tdTomato-KEULE and EGFP-
617 TUA5 were imaged and 2 second intervals in experiments featuring tdTomato-KEULE together
618 with Citrine-CESA6. All light energies were approximately 4 mW as measured at the end of the
619 optical fiber entering the confocal head. For high-speed acquisitions of tdTomato-KEULE,
620 image streaming was performed at an acquisition rate of 5 Hz (200 ms exposures). The focal
621 plane in all experiments was stabilized by hardware Adaptive Focus Control (Leica) to mitigate
622 changes in specimen intensity over time caused by thermal and mechanical drift in focus.
623 Photobleaching was performed by a Vector laser scanning unit (Intelligent Imaging
624 Innovations) integrated into the setup above at the right camera port. Focused laser light was
625 pulsed and scanned (pulse duration = 10 ms, raster block size = 20 units) on the image plane by a
626 pair of galvanometer-driven mirrors inside the Vector unit. Scanner positions were calibrated to
627 image coordinates using an automated procedure in Slidebook software (Intelligent Imaging
628 Innovations). Citrine photobleaching was performed using the 488 nm laser at the same power as
629 used for imaging but focused on the image plane. Areas of ~200 μm^2 were bleached in 20-30 s.
630 All imaging was performed on the upper hypocotyl cells (1-2 mm below the apical hook).
631 Specimen mounting was performed as described previously[69].
632
633 Image registration
634 To correct for lateral specimen drift in the movies, we performed image registration in
635 MATLAB. We first performed a running average on the image sequence using a three-frame
636 window (yielding an image series 2 frames shorter than the original series). We then performed
637 an intensity-based image registration algorithm using the MATLAB function imregtform, using
638 tformtype "translation" and conserving the pixel size. To minimize interpolation artifacts, we
639 first determined the transformation matrix that yielded the best intensity match for each
640 consecutive image pair, then calculated the cumulative transformation matrix for the whole
641 averaged image series and applied it to the original movie that was not frame averaged, minus
642 the first and last frame that were lost because of the frame averaging. Some of the KEULE-
643 tdTomato and Citrine-CESA colocalization movies (3 out of 8) still exhibited sample drift after

intensity-based registration. In those cases, we applied a feature-based method employing the locations of detected KEULE spots (See Methods: Particle Tracking for details) as registration features and using the MATLAB function estgeotform2d and a rigid transform.

KEULE particle tracking, streaming experiments, image series with labeled microtubules

Particle detection and tracking was performed on the registered movies. For streaming experiments and experiments featuring labeled microtubules (1 second time intervals) we used µTrack[49] to detect and estimate the positions of tdTomato-KEULE clusters in each frame and subsequently link detected foci from frame to frame to track individual KEULE clusters over time. For each experiment type, we used the following parameters:

Streaming image series.

For detection: initial psfSigma = 1.2 pixels, alpha for local max 0.05 and 10 max iterations for psfSigma estimation.

For tracking: max detection gap = 2 frames, min track length = 4 frames, max search radius = 2 pixels, gap penalty = 4.

1-second interval image series.

For detection: initial psfSigma = 1.2 pixels, alpha for local max 0.05 and 10 max iterations for psfSigma estimation.

For tracking: max detection gap = 1 frame, min track length = 1 frames, max search radius = 3 pixels, gap penalty = 4.

KEULE and CESA particle tracking in dual labeled movies

In experiments assessing KEULE localization and dynamics with respect to cellulose synthase complex (CSC) trafficking and we used the Spots module in Imaris software (Bitplane) to detect and track both tdTomato-KEULE clusters and Citrine-CESA6 particles. The Imaris Spots detector and filters performed better for Citrine-CESA6 signals, in particular. CSCs as labeled by Citrine-CESA6 were detected using a size value of 0.3 µm and quality value of 110. Tracking was performed by applying the Autoregressive Motion algorithm (maximum distance = 0.35 µm, maximum gap size = 2 frames). Successful deliveries of CSC complexes to the cell membrane were determined by dynamic criteria as described previously[7]. Briefly, a delivery event was defined when puncta that were mobile in the streaming cytosol (1) stabilized positionally in the optical plane of the plasma membrane, and (2) showed a transition to slow, steady and linear movement in the velocity range (~200-450 nm/min) we previously have determined be characteristic of CSC's actively synthesizing and extruding cellulose fibers into the cell wall[53]. To make this assessment, we first filtered CSC tracks by duration (>30 seconds), then used a custom GUI in MATLAB to manually inspect and verify each Spots track and associated image data for these characteristics. As a part of this process, the frame in which a tracked particle first showed evidence of stabilized lateral position was marked as the "tethering" frame – the frame showing the time and location of first stable interaction with the cell cortex of a presumed vesicle carrying one or more labeled CSC's.

Clusters of tdTomato-KEULE were detected with Spots module using a size parameter value of 0.3 µm, a quality value of 100 and were tracked using the Connected Components algorithm (frame to frame displacements of KEULE signal are small and not auto-correlated). These settings adequately detected and tracked KEULE clusters based on visual inspection of the results.

690
691 Maximum Likelihood Gaussian fitting for particles
692 We employed maximum likelihood Gaussian fitting as described in Mortensen et al.[50] to
693 use photon counts in estimating the accuracy of particle position and shape. To determine the
694 number of photons collected in each image pixel, we first needed to calibrate our camera gain
695 (photoelectrons per grey value or ADU). Photon detection can be modeled as a Poisson process,
696 which creates a distribution in which the mean equals the variance. Therefore, the camera gain is
697 equal to the coefficient between the mean and variance of the gray values in the image. To
698 calculate this coefficient, we first measured the noise floor of the camera by taking the average
699 of the gray values (intensity) of images acquired with the camera capped. We then determined
700 the grey value variance by subtracting one image from the other then calculating the variance
701 among these pixel-by-pixel difference values. To obtain the final variance, we divided this
702 number by 2 to account for the fact we are using two images for determining the differences.
703 Finally, we calculated the mean intensity of the images, subtracted the noise floor, and divided
704 by the variance to estimate the camera gain.
705 For each time point in every track, we cropped out a pixel grid with the estimated center
706 of the detected KEULE spot in the middle pixel (9 x 9 pixels). Along with a cropped image, the
707 fitting routine requires a set of initial parameters: xCoordinate, yCoordinate, point spread
708 function standard deviation (PSF SD), background, and an estimate of number of photons that
709 comprise the imaged PSF. The x- and y-coordinates we used are the estimates of position from
710 the particle tracking described above. Based on the approximate emission wavelength and
711 objective numerical aperture, we used 133 nm for the initial standard deviation of the PSF. We
712 estimated the background by calculating the median intensity of the outer border of the pixel grid
713 used for fitting after subtraction of the camera noise floor. If the center of the point source is in
714 the middle of the pixel and the PSF SD is 133 nm, we expect 0.16 of the photoelectrons to be in
715 the center pixel. Therefore, we estimated the number of photoelectrons in the imaged spot by
716 first subtracting the noise floor and pixel background from the intensity in the center pixel and
717 multiplying the result by 1/0.16 (6.25). Before performing fitting using these initial data, we
718 needed to address noise that could have been introduced by bilinear interpolation during the
719 image registration that was employed to mitigate specimen drift. To accomplish this, we used
720 the transformation matrix from registration to map the locations of the tracked particles back to
721 the locations in the original image sequence, we then performed MLE fitting on the non-
722 interpolated images by employing the method of Mortenson et al. [50] in MATLAB.
723 Since we used free fit parameters and there is noise in the data from photon counting, free
724 fluorescently tagged proteins, high local particle densities and unresolved distributions of labeled
725 structures, we excluded distance measurement from fits that were outside the expected parameter
726 ranges. In the case of the SD of the 2D Gaussian, we found that there was a distinct population
727 where the SD fit parameter was < 50 nm. Since our pixels correspond to 133 nm, in these fits all
728 the photoelectrons are contained in one pixel, which is not consistent for a diffraction-limited
729 spot at the magnification onto our camera (roughly 4 pixels). Similarly, we found that fit SD
730 values above 2x the estimated PSF SD in most cases represented a fit containing more than one
731 particle. Therefore, SD fit results with SD values outside 50 to 266 nm were excluded from
732 position measurements. Fit results with estimated numbers of photoelectrons > 1000 were also
733 considered outliers and excluded. Finally, high local particle densities the distance in some cases
734 caused the MLEwG fit to center on a nearby particle and not the particle marked by the starting
735 position. We therefore also did not include position information for fits where the distance

between the original estimate and the MLEwG position differed more than 2 x 133 nm. See Fig S6 for fit parameters for the tdTomato-KEULE clusters and CIT-CESA6 labeled CSCs.

KEULE to microtubule distance measurements

To determine the position of each KEULE spot to assess the spatial relationship of KEULE accumulation with the microtubule cytoskeleton we first determined the single frame with the highest number of measured photoelectrons for each KEULE track. For tracks that were longer than 4 frames we determined the max number of photoelectrons using a running three frames average, for shorter tracks we did not use frame averaging. The rational for this selection was two-fold. First, we reasoned that maximum signal might best be associated with the site of KEULE function, with initial signal rise being indicative of KEULE recruitment and/or assembly into a membrane fusion structure, and signal loss indicating KEULE disassociation or disassembly of the fusion machinery. Second, the precision of estimated position is proportional to photon sampling. It is also relevant to note that frame-to-frame movement of KEULE tracks were small (Fig. S7).

To locate positions of microtubule signal relative to each KEULE track location, we used a rotating linear filter combined with analysis of signal peaks and a two-step fitting procedure. At the coordinates of KEULE signal in each max value frame we drew a line 21 pixels long and 1 pixel wide extending 10.5 pixels to each side of the KEULE position and repeated this process in increments of 9 degrees to cover 360 degrees (Fig 4C). We then projected this array of lines on the microtubule channel and extracted the intensities (in photons) along each line at 1-pixel (133 nm) intervals by bilinear interpolation. To locate potential positions of microtubule signal along each sampling angle we used the MATLAB function Findpeaks with a MinPeakProminence of 25 to identify signal peaks. The 10.5-pixel distance is typically long enough to contain the peak intensity of the nearest microtubule. In fact, in many cases this length intersects multiple microtubules, but it is also possible for the end of the lines to partially intersect a microtubule with a peak outside the 10.5 pixels. For subsequent fitting steps, we included pixels from the center until the furthest peak on each side plus 3 pixels to catch the shoulder of these peaks, and at the same time, exclude signal from microtubules whose peaks are just outside the 10.5 pixel range from influencing the fitting. We then estimated the center position of each signal peak by modifying the 2D MLEwG[50] to a quasi-1D version, modeling the microtubule as a Gaussian wall[82] that is one pixel wide, as shown in the formula below.

(Formula 1)

$$\mathrm{N}\left(\frac{1}{\sqrt{2\pi\sigma^2}}\right)\left(\frac{1}{a}\right)\exp\left(-\frac{(x-\mu_x)^2}{2\sigma^2}\right)+b^2$$

Where:

N = number of photoelectrons

σ = Standard deviation

a = nm per pixel

x = position on the line

μ_x = center position

b = background photoelectrons

We found up to four peaks on a single line and fitted all peaks simultaneously by adding an additional term describing each additional peak as follows:

(Formula 2)

$$N_{\text{first}}\left(\frac{1}{\sqrt{2\pi\sigma_{\text{first}}^2}}\right)\left(\frac{1}{a}\right)\exp\left(-\frac{(x-\mu_{x\ \text{first}})^2}{2\sigma_{\text{first}}^2}\right)+$$

(Formula 3)

$$N_{\text{second}}\left(\frac{1}{\sqrt{2\pi\sigma_{\text{second}}^2}}\right)\left(\frac{1}{a}\right)\exp\left(-\frac{(x-\mu_{x\ \text{second}})^2}{2\sigma_{\text{second}}^2}\right)+b_{\text{global}}^2$$

For estimating the seeding parameters for the fit, we used the center of the maximum value pixel for each peak identified by Findpeaks. We used 160 nm (median value of the peak population) as the estimate for the standard deviation and we approximated the background by taking the square root of the lowest 10 percentile of all the pixels for all angles after subtracting the noise floor.

After fitting all microtubule peaks along all angular steps, we determined the distance from the KEULE location to the center of the nearest microtubule signal. We did this in three steps. First, we determined the nearest microtubule signal peak to the KEULE location from among the initial angular samples. Second, we determined the angle of the microtubule identified by the closest peak. Measuring the distance from the KEULE location to the center of the microtubule signal is most accurate along a line perpendicular from the KEULE location to the microtubule. By determining the local microtubule signal angle, we could then determine the optimal perpendicular sample angle. To find the local orientation of the microtubule we rotated a line of 21 pixels long around the center of the location where we initially found the closest microtubule peak. We extracted the summed signal intensities along these lines and determined the angle at which we found the maximum intensity, corresponding to the microtubule angle[69]. Finally, once we established the microtubule angle, we used the angle perpendicular to that microtubule angle to extract the nearest microtubule fit for the representative KEULE position. Distance values where the fit parameters for the microtubule positions were the number of photoelectrons were < 50 or > 10000, as well as SD fit parameters < 50 or > 250 nm were excluded from distance measurements. We required all the microtubule fits on the line to be within these parameters to be included in the analysis. See Fig. S8 (A to C) for fit parameters for KEULE (A) and microtubule signal (B) fits after selection as well as the standard error of the distance measurement between them (C).

Analysis of KEULE localization with CESA6 delivery sites

KEULE and CESA6 spots were detected and tracked in Imaris as described above and maximum likelihood 2D Gaussian fitting was applied to each set of tracks. CESA tracks tend to be relatively long and can be confounded by a dynamic background produced by highly motile CESA containing organelles including Golgi bodies and Trans-Golgi network compartments.

818 This background makes fully automated detection and quantitation of CSC delivery events
819 challenging. We therefore designed a graphical user interface in MATLAB that allowed us to
820 efficiently curate potential CESA6 delivery events identified in Imaris and verify whether
821 individual tracks were indeed depicting a CESA6 delivery. We have shown previously that
822 CESA delivery to the plasma membrane typically shows three distinct phases; (1) erratic
823 movement of CESA containing vesicles as they appear in the optical plane at the cell cortex, (2)
824 positional-stabilization and (3) slow and steady movement with typically linear trajectories. We
825 speculate that the second phase represents molecular tethering at the cell membrane and the
826 events that lead to vesicle fusion and cargo delivery. The third phase is behavior that we have
827 shown is characteristic of active CSC complexes in the plasma membrane as they synthesize
828 cellulose[53]. Thus, observation of this latter behavior indicates successful delivery of CESA
829 cargo to the cell membrane. For each CESA track that showed these three distinct phases, we
830 marked the first frame of CESA stabilization at the plasma membrane. From this position, we
831 determined the distance to the nearest KEULE spot in a 30-frame time range (60 seconds). Some
832 degree of coincidence between CESA deliveries and KEULE spots is expected by chance alone,
833 especially since the density of KEULE clusters at the plasma membrane is relatively high. To
834 evaluate whether the observed distribution of KEULE locations with sites of CESA stabilization
835 might be due to chance alone, we generated random positions in the same regions of interest
836 used for the experimental data and calculated the distances to the nearest KEULE spot. We used
837 these simulated data to model the expected distribution of distances and compared this
838 distribution to the distribution of distances found for confirmed CESA delivery events. First, we
839 divided both the experimental and simulated distance distributions up into 40 nm distance bins
840 and calculated the bin-by-bin count frequencies by the total number of simulated counts. We
841 then introduced a bias parameter δ that equates an observed frequency in each distance bin to the
842 expected value from the simulated distance bin as shown in formula (4).
843
844 (Formula 4)

$$P_{inDistBin}(\delta) = \frac{\text{Expected}_{inDistBin}\,\delta}{Expected_{\text{inDistBin}}\,\delta + \text{Expected}_{\text{outsideDistBin}}(1-\delta)}$$

845
846 The value of δ may vary between 0 and 1. For a possible observed frequency that equals
847 the expected frequency, δ is equal 0.5. If δ is greater than 0.5, an observed frequency is higher
848 than expected. Likewise, if δ is less than 0.5 the observed frequency lower than expected under
849 the null hypothesis. Use of the parameter allows us to use a Bayesian approach to test multiple
850 hypotheses to ask what bias value best may best explain the actual observed frequencies. To do
851 this, we calculated the Likelihood Ratio of observing an experimental result given a range of
852 values for δ (in increments of 0.001, excluding 0) for each frequency bin:
853
854 (Formula 5)

$$\frac{L(\delta)}{L\frac{1}{2}} = \frac{P_{inDistBin}\,(\delta)^{M}\,(1\,-\,P_{inDistBin}\,(\delta)^{N-M})}{Expected^{N}_{inDistBin}\,Expected^{N-M}_{outsideDistBin}}$$

855 Where:
856 $L(\delta)$ = likelihood of the data given the bias δ,
857 $L\frac{1}{2}$ = likelihood of the data in the neutral case (no positive or negative bias)
858 N = total number of measurements

M = number of measurements in this specific distance bin

We then found the maximum a posteriori probability (MAP) for δ and computed the shortest range of δ values for the highest posterior density (HPD) that contains 95% of the normalized probability density. Maximum likelihood estimates for δ below 0.5 indicate underrepresentation at the distance of interest and above 0.5 indicate overrepresentation of experimental data compared to the unbiased case.

Analysis of KEULE localization with microtubules

We used the same Bayesian approach describe above for analyzing the localization of KEULE clusters with respect to the estimated center of the nearest microtubule. We changed the distance bin size from 40 to 20 nm.

Hot spot analysis

To investigate if some KEULE events are independent of each other each or not (e.g. if "hot spots" for KEULE accumulation may exist), we examined colocalization between sequential KEULE spots in time series collected from cells expressing both labeled KEULE and tubulin proteins. Within a region of interest in each time series, we selected all KEULE tracks that were first detected between frames 2 and 31 and calculated the distance to all other KEULE tracks that started subsequently up to and including frame 301. For position estimates we used the frame in the track that showed the highest number of fitted photoelectrons. To compare the degree of colocalization of the initial KEULE tracks with future KEULE tracks to that expected from chance alone, we created a simulated initial dataset with random locations within the same region of interest and calculated the distances to all KEULE tracks in the same time range.

Since KEULE foci are positionally stable we chose a stringent distance threshold of 133 nm (1 pixel) to declare two spots or locations to be co-localized. Because of the relatively high density of KEULE spots at the plasma membrane, colocalization is expected at some point in time, therefore the time frame of colocalization analysis is also important. Indeed, we observe a large degree of colocalization in the whole dataset for both the experimental and simulated data, but with very distinct waiting time distributions (Fig. S5D). Based on the differences in the distribution of waiting times between random simulated positions and KEULE positions until the next KEULE spot arrives, we determined that a 40 second time delay window captures most biologically relevant colocalizations while excluding most random colocalizations due to KEULE density and chance.

1. Noordstra, I., and Akhmanova, A. (2017). Linking cortical microtubule attachment and exocytosis. F1000Research *6*, 469. https://doi.org/10.12688/f1000research.10729.1.

2. Spiliotis, E.T., and Nelson, W.J. (2003). Spatial control of exocytosis. Curr. Opin. Cell Biol. *15*, 430–437. https://doi.org/10.1016/s0955-0674(03)00074-7.

3. Fourriere, L., Jimenez, A.J., Perez, F., and Boncompain, G. (2020). The role of microtubules in secretory protein transport. Journal of Cell Science *133*, jcs237016. https://doi.org/10.1242/jcs.237016.

4. Chang, F., and Martin, S.G. (2009). Shaping Fission Yeast with Microtubules. Cold Spring Harb. Perspect. Biol. *1*, a001347. https://doi.org/10.1101/cshperspect.a001347.

5. Bartolini, F., and Gundersen, G.G. (2006). Generation of noncentrosomal microtubule arrays. J. Cell Sci. *119*, 4155–4163. https://doi.org/10.1242/jcs.03227.

6. Shaw, S.L., Kamyar, R., and Ehrhardt, D.W. (2003). Sustained Microtubule Treadmilling in Arabidopsis Cortical Arrays. Science *300*, 1715–1718. https://doi.org/10.1126/science.1083529.

7. Gutierrez, R., Lindeboom, J.J., Paredez, A.R., Emons, A.M.C., and Ehrhardt, D.W. (2009). Arabidopsis cortical microtubules position cellulose synthase delivery to the plasma membrane and interact with cellulose synthase trafficking compartments. Nat. Cell Biol. *11*, 797–806. https://doi.org/10.1038/ncb1886.

8. Sampathkumar, A., Gutierrez, R., McFarlane, H.E., Bringmann, M., Lindeboom, J., Emons, A.-M., Samuels, L., Ketelaar, T., Ehrhardt, D.W., and Persson, S. (2013). Patterning and Lifetime of Plasma Membrane-Localized Cellulose Synthase Is Dependent on Actin Organization in Arabidopsis Interphase Cells. Plant Physiol. *162*, 675–688. https://doi.org/10.1104/pp.113.215277.

9. Vellosillo, T., Dinneny, J.R., Somerville, C.R., and Ehrhardt, D.W. (2021). TRANVIA (TVA) facilitates cellulose synthase trafficking and delivery to the plasma membrane. Proc. Natl. Acad. Sci. *118*, e2021790118. https://doi.org/10.1073/pnas.2021790118.

10. Gutierrez, R., Lindeboom, J.J., Paredez, A.R., Emons, A.M.C., and Ehrhardt, D.W. (2009). Arabidopsis cortical microtubules position cellulose synthase delivery to the plasma membrane and interact with cellulose synthase trafficking compartments. Nature Cell Biology *11*, 797–806. https://doi.org/10.1038/ncb1886.

11. Li, S., Lei, L., Somerville, C.R., and Gu, Y. (2012). Cellulose synthase interactive protein 1 (CSI1) links microtubules and cellulose synthase complexes. Proc. Natl. Acad. Sci. *109*, 185–190. https://doi.org/10.1073/pnas.1118560109.

928 12. Bringmann, M., Li, E., Sampathkumar, A., Kocabek, T., Hauser, M.-T., and Persson, S.
929 (2012). POM-POM2/CELLULOSE SYNTHASE INTERACTING1 Is Essential for the
930 Functional Association of Cellulose Synthase and Microtubules in Arabidopsis. Plant Cell *24*,
931 163–177. https://doi.org/10.1105/tpc.111.093575.

932 13. Zhu, X., Li, S., Pan, S., Xin, X., and Gu, Y. (2018). CSI1, PATROL1, and exocyst complex
933 cooperate in delivery of cellulose synthase complexes to the plasma membrane. Proc. Natl.
934 Acad. Sci. *115*, E3578–E3587. https://doi.org/10.1073/pnas.1800182115.

935 14. Lei, L., Singh, A., Bashline, L., Li, S., Yingling, Y.G., and Gu, Y. (2015). CELLULOSE
936 SYNTHASE INTERACTIVE1 Is Required for Fast Recycling of Cellulose Synthase Complexes
937 to the Plasma Membrane in Arabidopsis. The Plant Cell *27*, 2926–2940.
938 https://doi.org/10.1105/tpc.15.00442.

939 15. Paredez, A.R., Somerville, C.R., and Ehrhardt, D.W. (2006). Visualization of Cellulose
940 Synthase Demonstrates Functional Association with Microtubules. Science *312*, 1491–1495.
941 https://doi.org/10.1126/science.1126551.

942 16. Gutierrez, R., Lindeboom, J.J., Paredez, A.R., Emons, A.M.C., and Ehrhardt, D.W. (2009).
943 Arabidopsis cortical microtubules position cellulose synthase delivery to the plasma membrane
944 and interact with cellulose synthase trafficking compartments. Nature Cell Biology *11*, 797–806.
945 https://doi.org/10.1038/ncb1886.

946 17. DeBolt, S., Gutierrez, R., Ehrhardt, D.W., Melo, C.V., Ross, L., Cutler, S.R., Somerville, C.,
947 and Bonetta, D. (2007). Morlin, an inhibitor of cortical microtubule dynamics and cellulose
948 synthase movement. Proc. Natl. Acad. Sci. *104*, 5854–5859.
949 https://doi.org/10.1073/pnas.0700789104.

950 18. Emons, A.M.C., Mulder, B.M., Emons, A.M.C., and Mulder, B.M. (2000). How the
951 deposition of cellulose microfibrils builds cell wall architecture. Trends Plant Sci. *5*, 35–40.
952 https://doi.org/10.1016/s1360-1385(99)01507-1.

953 19. Hamant, O., Heisler, M.G., Jönsson, H., Krupinski, P., Uyttewaal, M., Bokov, P., Corson, F.,
954 Sahlin, P., Boudaoud, A., Meyerowitz, E.M., et al. (2008). Developmental Patterning by
955 Mechanical Signals in Arabidopsis. Science *322*, 1650–1655.
956 https://doi.org/10.1126/science.1165594.

957 20. Zhang, B., Karnik, R., Alvim, J., Donald, N., and Blatt, M.R. (2019). Dual Sites for SEC11
958 on the SNARE SYP121 Implicate a Binding Exchange during Secretory Traffic1. Plant Physiol
959 *180*, 228–239. https://doi.org/10.1104/pp.18.01315.

960 21. Honsbein, A., Sokolovski, S., Grefen, C., Campanoni, P., Pratelli, R., Paneque, M., Chen, Z.,
961 Johansson, I., and Blatt, M.R. (2009). A tripartite SNARE-K+ channel complex mediates in
962 channel-dependent K+ nutrition in Arabidopsis. Plant Cell *21*, 2859–2877.
963 https://doi.org/10.1105/tpc.109.066118.

964 22. Assaad, F.F., Qiu, J.-L., Youngs, H., Ehrhardt, D., Zimmerli, L., Kalde, M., Wanner, G.,
965 Peck, S.C., Edwards, H., Ramonell, K., et al. (2004). The PEN1 Syntaxin Defines a Novel
966 Cellular Compartment upon Fungal Attack and Is Required for the Timely Assembly of Papillae.
967 Mol. Biol. Cell *15*, 5118–5129. https://doi.org/10.1091/mbc.e04-02-0140.

968 23. Bloch, D., Pleskot, R., Pejchar, P., Potocký, M., Trpko¡ová, P., Cwiklik, L., Vuka¡inović, N.,
969 Sternberg, H., Yalovsky, S., and Žárský, V. (2016). Exocyst SEC3 and Phosphoinositides Define
970 Sites of Exocytosis in Pollen Tube Initiation and Growth. Plant Physiol. *172*, 980–1002.
971 https://doi.org/10.1104/pp.16.00690.

972 24. Fendrych, M., Synek, L., Pečenková, T., Drdová, E.J., Sekereš, J., Rycke, R. de, Nowack,
973 M.K., and Žárský, V. (2013). Visualization of the exocyst complex dynamics at the plasma
974 membrane of Arabidopsis thaliana. MBoC *24*, 510–520. https://doi.org/10.1091/mbc.e12-06-
975 0492.

976 25. Barg, S., Knowles, M.K., Chen, X., Midorikawa, M., and Almers, W. (2010). Syntaxin
977 clusters assemble reversibly at sites of secretory granules in live cells. Proceedings of the
978 National Academy of Sciences *107*, 20804–20809. https://doi.org/10.1073/pnas.1014823107.

979 26. Knowles, M.K., Barg, S., Wan, L., Midorikawa, M., Chen, X., and Almers, W. (2010).
980 Single secretory granules of live cells recruit syntaxin-1 and synaptosomal associated protein 25
981 (SNAP-25) in large copy numbers. Proceedings of the National Academy of Sciences *107*,
982 20810–20815. https://doi.org/10.1073/pnas.1014840107.

983 27. McNew, J.A., Weber, T., Parlati, F., Johnston, R.J., Melia, T.J., Söllner, T.H., and Rothman,
984 J.E. (2000). Close Is Not Enough. The Journal of Cell Biology *150*, 105–118.
985 https://doi.org/10.1083/jcb.150.1.105.

986 28. Südhof, T.C., and Rothman, J.E. (2009). Membrane Fusion: Grappling with SNARE and SM
987 Proteins. Science *323*, 474–477. https://doi.org/10.1126/science.1161748.

988 29. Burgoyne, R.D., Barclay, J.W., Ciufo, L.F., Graham, M.E., Handley, M.T.W., and Morgan,
989 A. (2009). The Functions of Munc18□1 in Regulated Exocytosis. Ann. N. York Acad. Sci. *1152*,
990 76–86. https://doi.org/10.1111/j.1749-6632.2008.03987.x.

991 30. Baker, R.W., Jeffrey, P.D., Zick, M., Phillips, B.P., Wickner, W.T., and Hughson, F.M.
992 (2015). A direct role for the Sec1/Munc18-family protein Vps33 as a template for SNARE
993 assembly. Science *349*, 1111–1114. https://doi.org/10.1126/science.aac7906.

994 31. Stepien, K.P., Prinslow, E.A., and Rizo, J. (2019). Munc18-1 is crucial to overcome the
995 inhibition of synaptic vesicle fusion by αSNAP. Nat. Commun. *10*, 4326.
996 https://doi.org/10.1038/s41467-019-12188-4.

997 32. Peng, R.-W., Guetg, C., Abellan, E., and Fussenegger, M. (2010). Munc18b regulates core
998 SNARE complex assembly and constitutive exocytosis by interacting with the N-peptide and the

999 closed-conformation C-terminus of syntaxin 3. Biochem. J. *431*, 353–361.
1000 https://doi.org/10.1042/bj20100145.

1001 33. Hashizume, K., Cheng, Y.-S., Hutton, J.L., Chiu, C., and Carr, C.M. (2009). Yeast Sec1p
1002 Functions before and after Vesicle Docking. Mol. Biol. Cell *20*, 4673–4685.
1003 https://doi.org/10.1091/mbc.e09-02-0172.

1004 34. Mayer, U., Ruiz, R.A.T., Berleth, T., Miséra, S., and Jürgens, G. (1991). Mutations affecting
1005 body organization in the Arabidopsis embryo. Nature *353*, 402–407.
1006 https://doi.org/10.1038/353402a0.

1007 35. Assaad, F.F., Mayer, U., Wanner, G., and Jürgens, G. (1996). The KEULE gene is involved
1008 in cytokinesis in Arabidopsis. Mol. Gen. Genet. MGG *253*, 267–277.
1009 https://doi.org/10.1007/pl00008594.

1010 36. Karnik, R., Grefen, C., Bayne, R., Honsbein, A., Köhler, T., Kioumourtzoglou, D., Williams,
1011 M., Bryant, N.J., and Blatt, M.R. (2013). Arabidopsis Sec1/Munc18 protein SEC11 is a
1012 competitive and dynamic modulator of SNARE binding and SYP121-dependent vesicle traffic.
1013 Plant Cell *25*, 1368–1382. https://doi.org/10.1105/tpc.112.108506.

1014 37. Karnik, R., Zhang, B., Waghmare, S., Aderhold, C., Grefen, C., and Blatt, M.R. (2015).
1015 Binding of SEC11 indicates its role in SNARE recycling after vesicle fusion and identifies two
1016 pathways for vesicular traffic to the plasma membrane. Plant Cell *27*, 675–694.
1017 https://doi.org/10.1105/tpc.114.134429.

1018 38. Karnahl, M., Park, M., Krause, C., Hiller, U., Mayer, U., Stierhof, Y.-D., and Jürgens, G.
1019 (2018). Functional diversification of Arabidopsis SEC1-related SM proteins in cytokinetic and
1020 secretory membrane fusion. Proceedings of the National Academy of Sciences *115*, 6309–6314.
1021 https://doi.org/10.1073/pnas.1722611115.

1022 39. Assaad, F.F., Huet, Y., Mayer, U., and Jürgens, G. (2001). The Cytokinesis Gene KEULE
1023 Encodes a Sec1 Protein That Binds the Syntaxin Knolle. The Journal of Cell Biology *152*, 531–
1024 544. https://doi.org/10.1083/jcb.152.3.531.

1025 40. Assaad, F.F., Mayer, U., Wanner, G., and Jürgens, G. (1996). The KEULE gene is involved
1026 in cytokinesis in Arabidopsis. Molecular and General Genetics MGG *253*, 267–277.
1027 https://doi.org/10.1007/pl00008594.

1028 41. Carr, C.M., Grote, E., Munson, M., Hughson, F.M., and Novick, P.J. (1999). Sec1p Binds to
1029 SNARE Complexes and Concentrates at Sites of Secretion. J. Cell Biol. *146*, 333–344.
1030 https://doi.org/10.1083/jcb.146.2.333.

1031 42. Scott, B.L., Komen, J.S.V., Irshad, H., Liu, S., Wilson, K.A., and McNew, J.A. (2004).
1032 Sec1p directly stimulates SNARE-mediated membrane fusion in vitro. J. Cell Biol. *167*, 75–85.
1033 https://doi.org/10.1083/jcb.200405018.

1034 43. Zilly, F.E., Sørensen, J.B., Jahn, R., and Lang, T. (2006). Munc18-Bound Syntaxin Readily
1035 Forms SNARE Complexes with Synaptobrevin in Native Plasma Membranes. PLoS Biol. *4*,
1036 e330. https://doi.org/10.1371/journal.pbio.0040330.

1037 44. Medine, C.N., Rickman, C., Chamberlain, L.H., and Duncan, R.R. (2007). Munc18-1
1038 prevents the formation of ectopic SNARE complexes in living cells. J. Cell Sci. *120*, 4407–4415.
1039 https://doi.org/10.1242/jcs.020230.

1040 45. Rickman, C., and Duncan, R.R. (2010). Munc18/Syntaxin Interaction Kinetics Control
1041 Secretory Vesicle Dynamics2. J. Biol. Chem. *285*, 3965–3972.
1042 https://doi.org/10.1074/jbc.m109.040402.

1043 46. Smyth, A.M., Rickman, C., and Duncan, R.R. (2010). Vesicle Fusion Probability Is
1044 Determined by the Specific Interactions of Munc18*. J. Biol. Chem. *285*, 38141–38148.
1045 https://doi.org/10.1074/jbc.m110.164038.

1046 47. Trexler, A.J., Sochacki, K.A., and Taraska, J.W. (2016). Imaging the recruitment and loss of
1047 proteins and lipids at single sites of calcium-triggered exocytosis. Mol. Biol. Cell *27*, 2423–2434.
1048 https://doi.org/10.1091/mbc.e16-01-0057.

1049 48. Somasundaram, A., and Taraska, J.W. (2018). Local protein dynamics during microvesicle
1050 exocytosis in neuroendocrine cells. Mol. Biol. Cell *29*, 1891–1903.
1051 https://doi.org/10.1091/mbc.e17-12-0716.

1052 49. Jaqaman, K., Loerke, D., Mettlen, M., Kuwata, H., Grinstein, S., Schmid, S.L., and Danuser,
1053 G. (2008). Robust single-particle tracking in live-cell time-lapse sequences. Nat. Methods *5*,
1054 695–702. https://doi.org/10.1038/nmeth.1237.

1055 50. Mortensen, K.I., Churchman, L.S., Spudich, J.A., and Flyvbjerg, H. (2010). Optimized
1056 localization analysis for single-molecule tracking and super-resolution microscopy. Nat.
1057 Methods *7*, 377–381. https://doi.org/10.1038/nmeth.1447.

1058 51. Haigler, C.H., and Brown, R.M. (1986). Transport of rosettes from the golgi apparatus to the
1059 plasma membrane in isolated mesophyll cells ofZinnia elegans during differentiation to tracheary
1060 elements in suspension culture. Protoplasma *134*, 111–120. https://doi.org/10.1007/bf01275709.

1061 52. Zhang, Y., Nikolovski, N., Sorieul, M., Vellosillo, T., McFarlane, H.E., Dupree, R., Kesten,
1062 C., Schneider, R., Driemeier, C., Lathe, R., et al. (2016). Golgi-localized STELLO proteins
1063 regulate the assembly and trafficking of cellulose synthase complexes in Arabidopsis. Nat.
1064 Commun. *7*, 11656. https://doi.org/10.1038/ncomms11656.

1065 53. Paredez, A.R., Somerville, C.R., and Ehrhardt, D.W. (2006). Visualization of Cellulose
1066 Synthase Demonstrates Functional Association with Microtubules. Science *312*, 1491–1495.
1067 https://doi.org/10.1126/science.1126551.

1068 54. Scheible, W.-R., Eshed, R., Richmond, T., Delmer, D., and Somerville, C. (2001).
1069 Modifications of cellulose synthase confer resistance to isoxaben and thiazolidinone herbicides
1070 in Arabidopsis Ixr1 mutants. Proceedings of the National Academy of Sciences *98*, 10079–
1071 10084. https://doi.org/10.1073/pnas.191361598.

1072 55. Zhou, Q., Lai, Y., Bacaj, T., Zhao, M., Lyubimov, A.Y., Uervirojnangkoorn, M., Zeldin,
1073 O.B., Brewster, A.S., Sauter, N.K., Cohen, A.E., et al. (2015). Architecture of the
1074 synaptotagmin–SNARE machinery for neuronal exocytosis. Nature *525*, 62–67.
1075 https://doi.org/10.1038/nature14975.

1076 56. Brunger, A.T. (2005). Structure and function of SNARE and SNARE-interacting proteins. Q
1077 Rev Biophys *38*, 1–47. https://doi.org/10.1017/s0033583505004051.

1078 57. Rothman, J.E., Krishnakumar, S.S., Grushin, K., and Pincet, F. (2017). Hypothesis –
1079 buttressed rings assemble, clamp, and release SNAREpins for synaptic transmission. FEBS Lett.
1080 *591*, 3459–3480. https://doi.org/10.1002/1873-3468.12874.

1081 58. Cho, W.J., Jeremic, A., and Jena, B.P. (2005). Size of Supramolecular SNARE Complex:
1082 Membrane-Directed Self-Assembly. J. Am. Chem. Soc. *127*, 10156–10157.
1083 https://doi.org/10.1021/ja052442m.

1084 59. Cho, W.J., Lee, J., Zhang, L., Ren, G., Shin, L., Manke, C.W., Potoff, J., Kotaria, N.,
1085 Zhvania, M.G., and Jena, B.P. (2011). Membrane directed molecular assembly of the neuronal
1086 SNARE complex. J. Cell. Mol. Med. *15*, 31–37. https://doi.org/10.1111/j.1582-
1087 4934.2010.01152.x.

1088 60. Giddings, T.H., and Staehelin, L.A. (1988). Spatial relationship between microtubules and
1089 plasma-membrane rosettes during the deposition of primary wall microfibrils in Closterium sp.
1090 Planta *173*, 22–30. https://doi.org/10.1007/bf00394482.

1091 61. Lindeboom, J.J., Nakamura, M., Saltini, M., Hibbel, A., Walia, A., Ketelaar, T., Emons,
1092 A.M.C., Sedbrook, J.C., Kirik, V., Mulder, B.M., et al. (2019). CLASP stabilization of plus ends
1093 created by severing promotes microtubule creation and reorientation. J. Cell Biol. *218*, 190–205.
1094 https://doi.org/10.1083/jcb.201805047.

1095 62. Crowell, E.F., Bischoff, V., Desprez, T., Rolland, A., Stierhof, Y.-D., Schumacher, K.,
1096 Gonneau, M., Höfte, H., and Vernhettes, S. (2009). Pausing of Golgi Bodies on Microtubules
1097 Regulates Secretion of Cellulose Synthase Complexes in Arabidopsis. Plant Cell *21*, 1141–1154.
1098 https://doi.org/10.1105/tpc.108.065334.

1099 63. Martinière, A., Gayral, P., Hawes, C., and Runions, J. (2011). Building bridges: formin1 of
1100 Arabidopsis forms a connection between the cell wall and the actin cytoskeleton. Plant J. *66*,
1101 354–365. https://doi.org/10.1111/j.1365-313x.2011.04497.x.

1102 64. Geelen, D., Leyman, B., Batoko, H., Sansebastiano, G.-P.D., Moore, I., and Blatt, M.R.
1103 (2002). The abscisic acid-related SNARE homolog NtSyr1 contributes to secretion and growth:

1104 evidence from competition with its cytosolic domain. Plant Cell *14*, 387–406.
1105 https://doi.org/10.1105/tpc.010328.

1106 65. Grefen, C., Chen, Z., Honsbein, A., Donald, N., Hills, A., and Blatt, M.R. (2010). A novel
1107 motif essential for SNARE interaction with the K(+) channel KC1 and channel gating in
1108 Arabidopsis. Plant Cell *22*, 3076–3092. https://doi.org/10.1105/tpc.110.077768.

1109 66. Hoffmann, N., King, S., Samuels, A.L., and McFarlane, H.E. (2021). Subcellular
1110 coordination of plant cell wall synthesis. Dev. Cell *56*, 933–948.
1111 https://doi.org/10.1016/j.devcel.2021.03.004.

1112 67. Cosgrove, D.J. (2015). Plant expansins: diversity and interactions with plant cell walls. Curr.
1113 Opin. Plant Biol. *25*, 162–172. https://doi.org/10.1016/j.pbi.2015.05.014.

1114 68. Baskin, T.I. (2005). ANISOTROPIC EXPANSION OF THE PLANT CELL WALL. Annu.
1115 Rev. Cell Dev. Biol. *21*, 203–222. https://doi.org/10.1146/annurev.cellbio.20.082503.103053.

1116 69. Lindeboom, J.J., Nakamura, M., Hibbel, A., Shundyak, K., Gutierrez, R., Ketelaar, T.,
1117 Emons, A.M.C., Mulder, B.M., Kirik, V., and Ehrhardt, D.W. (2013). A Mechanism for
1118 Reorientation of Cortical Microtubule Arrays Driven by Microtubule Severing. Science *342*,
1119 1245533. https://doi.org/10.1126/science.1245533.

1120 70. Baas, P.W., Rao, A.N., Matamoros, A.J., and Leo, L. (2016). Stability properties of neuronal
1121 microtubules. Cytoskeleton *73*, 442–460. https://doi.org/10.1002/cm.21286.

1122 71. Tojima, T., Itofusa, R., and Kamiguchi, H. (2014). Steering Neuronal Growth Cones by
1123 Shifting the Imbalance between Exocytosis and Endocytosis. The Journal of Neuroscience *34*,
1124 7165–7178. https://doi.org/10.1523/jneurosci.5261-13.2014.

1125 72. Brown, A.-L., Wilkins, O.G., Keuss, M.J., Hill, S.E., Zanovello, M., Lee, W.C., Bampton,
1126 A., Lee, F.C.Y., Masino, L., Qi, Y.A., et al. (2022). TDP-43 loss and ALS-risk SNPs drive mis-
1127 splicing and depletion of UNC13A. Nature *603*, 131–137. https://doi.org/10.1038/s41586-022-
1128 04436-3.

1129 73. Ma, X.R., Prudencio, M., Koike, Y., Vatsavayai, S.C., Kim, G., Harbinski, F., Briner, A.,
1130 Rodriguez, C.M., Guo, C., Akiyama, T., et al. (2022). TDP-43 represses cryptic exon inclusion
1131 in the FTD–ALS gene UNC13A. Nature *603*, 124–130. https://doi.org/10.1038/s41586-022-
1132 04424-7.

1133 74. Liu, X., and Henty-Ridilla, J.L. (2022). Multiple roles for the cytoskeleton in ALS. Exp.
1134 Neurol. *355*, 114143. https://doi.org/10.1016/j.expneurol.2022.114143.

1135 75. Zhang, S., Cooper-Knock, J., Weimer, A.K., Shi, M., Moll, T., Marshall, J.N.G., Harvey, C.,
1136 Nezhad, H.G., Franklin, J., Souza, C. dos S., et al. (2022). Genome-wide identification of the
1137 genetic basis of amyotrophic lateral sclerosis. Neuron *110*, 992-1008.e11.
1138 https://doi.org/10.1016/j.neuron.2021.12.019.

76. Curtis, M.D., and Grossniklaus, U. (2003). A Gateway Cloning Vector Set for High-Throughput Functional Analysis of Genes in Planta. Plant Physiol. *133*, 462–469. https://doi.org/10.1104/pp.103.027979.

77. Shaner, N.C., Campbell, R.E., Steinbach, P.A., Giepmans, B.N.G., Palmer, A.E., and Tsien, R.Y. (2004). Improved monomeric red, orange and yellow fluorescent proteins derived from Discosoma sp. red fluorescent protein. Nat. Biotechnol. *22*, 1567–1572. https://doi.org/10.1038/nbt1037.

78. Kirik, V., Herrmann, U., Parupalli, C., Sedbrook, J.C., Ehrhardt, D.W., and Hülskamp, M. (2007). CLASP localizes in two discrete patterns on cortical microtubules and is required for cell morphogenesis and cell division in Arabidopsis. J. Cell Sci. *120*, 4416–4425. https://doi.org/10.1242/jcs.024950.

79. Assaad, F.F., Huet, Y., Mayer, U., and Jürgens, G. (2001). The Cytokinesis Gene KEULE Encodes a Sec1 Protein That Binds the Syntaxin Knolle. J. Cell Biol. *152*, 531–544. https://doi.org/10.1083/jcb.152.3.531.

80. Clough, S.J., and Bent, A.F. (1998). Floral dip: a simplified method for Agrobacterium mediated transformation of Arabidopsis thaliana. Plant J. *16*, 735–743. https://doi.org/10.1046/j.1365-313x.1998.00343.x.

81. Logemann, E., Birkenbihl, R.P., Ülker, B., and Somssich, I.E. (2006). An improved method for preparing Agrobacterium cells that simplifies the Arabidopsis transformation protocol. Plant Methods *2*, 16. https://doi.org/10.1186/1746-4811-2-16.

82. Ruhnow, F., Zwicker, D., and Diez, S. (2011). Tracking Single Particles and Elongated Filaments with Nanometer Precision. Biophys. J. *100*, 2820–2828. https://doi.org/10.1016/j.bpj.2011.04.023.

Acknowledgments: We thank Michael Davidson for the kind gift of the tdTomato construct. We thank Zdeněk Lánský, Johnathan Cooper-Knock and Masayoshi Nakamura for advice and insightful comments.

Funding:

National Institutes of Health grant R15GM137247-01 (VK)

National Institutes of Health grant R01GM123259-01 (DWE)

Author contributions:

Conceptualization: JJL, RG, VK, DWE

Methodology: JJL, RG, VK, DWE

Investigation: JJL, RG, VK, DWE

Visualization: JJL, RG, DWE

Funding acquisition: VK, DWE

Writing – original draft: JJL, RG, DWE

Writing – review & editing: JJL, RG, VK, DWE

Competing interests: The authors declare no competing interests.

Data and materials availability: Biological material, raw data, processed data and MATLAB scripts used for the analysis are available upon request.

Figures

Figure 1

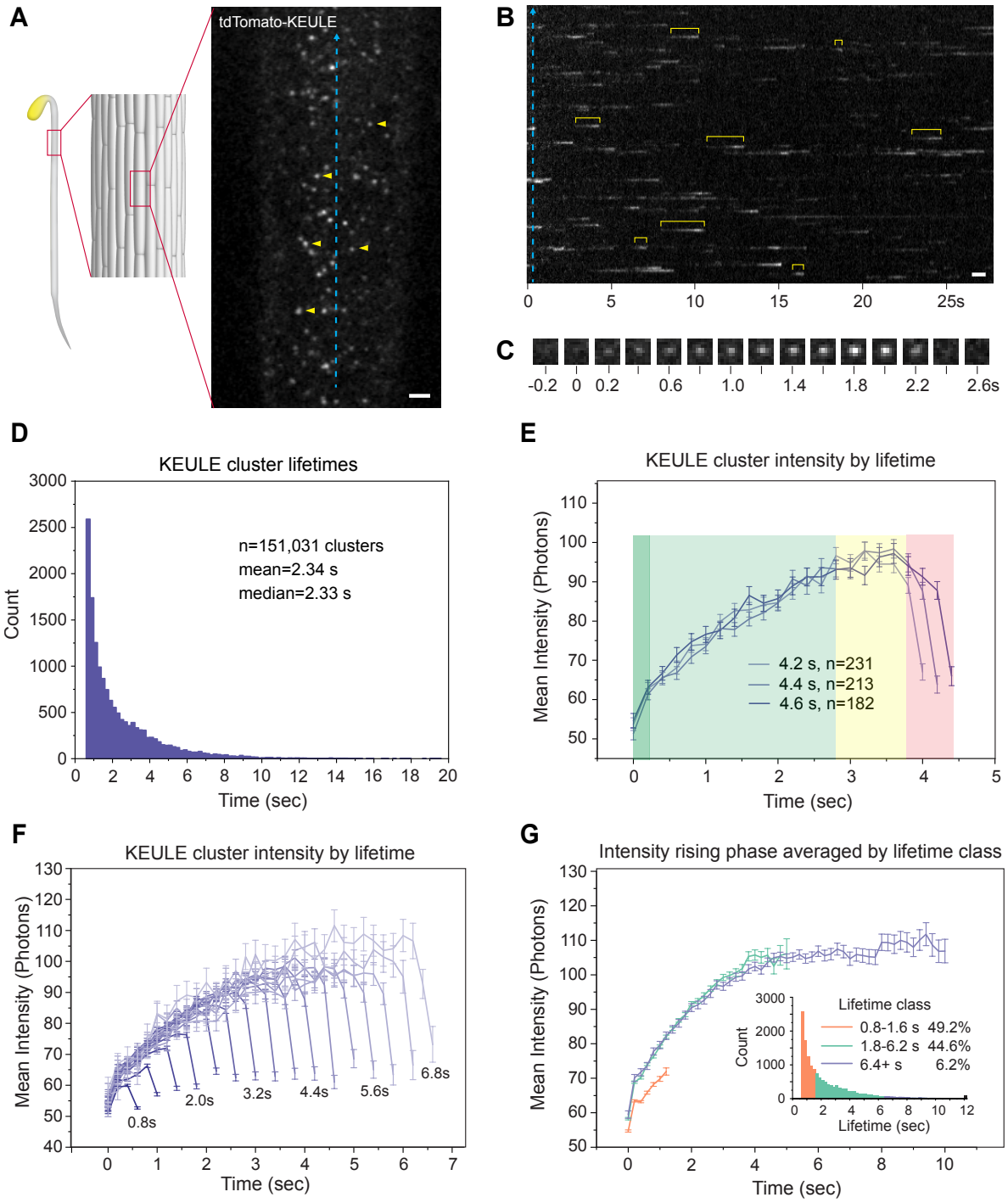

1185 **Fig. 1. KEULE assembly dynamics at the plasma membrane**. (**A**) Distribution of tdTomato-KEULE
1186 signal at the plasma membrane of etiolated hypocotyl cells in *Arabidopsis*. Arrowheads point out
1187 individual clusters of labeled KEULE protein. (**B**) Kymograph of the tdTomato-KEULE signal intensity
1188 over time as sampled over the transect line shown in (**A**) (blue dashes). The yellow brackets highlight
1189 several individual tdTomato-KEULE clusters. (**C**) Example of tdTomato-KEULE cluster intensity over
1190 time. (**D**) Histogram of KEULE cluster lifetimes in 200 ms bins. (**E**) Average tdTomato-KEULE cluster
1191 signal intensity with a lifetime of 4.2, 4.4 and 4.6 s. Note the initial rapid increase in signal over the first
1192 acquisition step (darker green), the more gradual, near linear, ramp up (green) to a plateau (yellow),
1193 followed by abrupt loss to non-detection (red). (**F**) Average tdTomato-KEULE cluster signal intensity
1194 with lifetimes ranging from 0.8 to 6.8 s. (**G**) Average signal intensities of tdTomato-KEULE clusters in
1195 three cumulative lifetime ranges, 0.8 to 1.6 s, 1.8 to 6.2 s and 6.4+ s. The inset shows the lifetime
1196 distribution histogram of tdTomato-KEULE cluster lifetimes with the lifetime ranges color coded. Data
1197 acquired from 12 cells on 12 seedlings. Error bars indicate S.E. Scale bars are 2 µm.

Figure 2

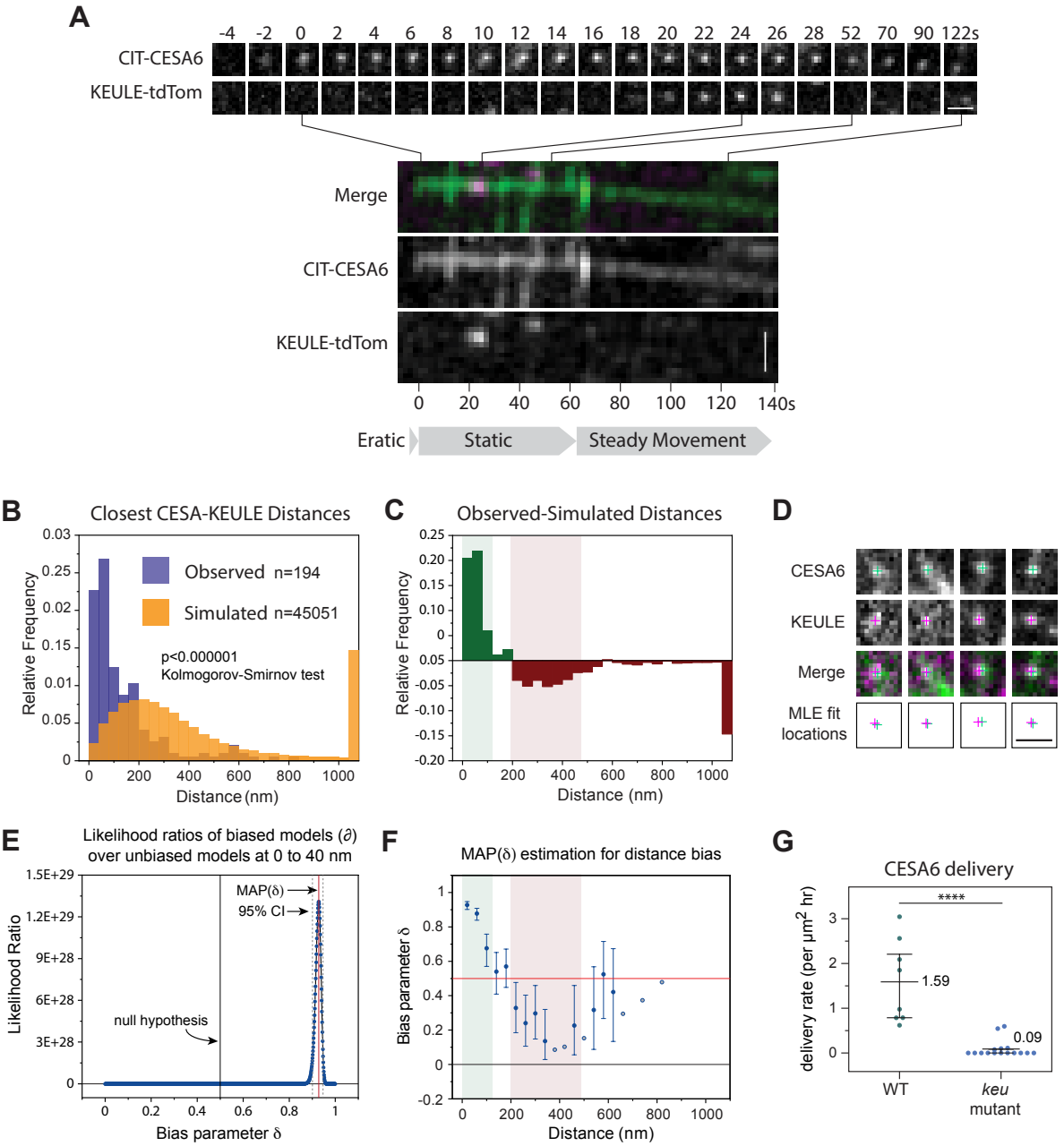
A
-4 -2 0 2 4 6 8 10 12 14 16 18 20 22 24 26 28 52 70 90 122s
CIT-CESA6
KEULE-tdTom
Merge
CIT-CESA6
KEULE-tdTom
0 20 40 60 80 100 120 140s
Eratic
Static
Steady Movement
B
Closest CESA-KEULE Distances
Observed n=194
Simulated n=45051
p<0.000001
Kolmogorov-Smirnov test
Relative Frequency
Distance (nm)
C
Observed-Simulated Distances
Relative Frequency
Distance (nm)
D
CESA6
KEULE
Merge
MLE fit locations
E
Likelihood ratios of biased models (∂) over unbiased models at 0 to 40 nm
MAP(δ)
95% CI
null hypothesis
Likelihood Ratio
Bias parameter δ
F
MAP(δ) estimation for distance bias
Bias parameter δ
Distance (nm)
G
CESA6 delivery
****
1.59
0.09
delivery rate (per μm² hr)
WT
keu mutant

1201 **Fig. 2. KEULE is spatially associated with and required for CSC delivery to the plasma membrane.**
1202 (**A**) CESA exocytosis event. (Top panel) Time series (top panel) and kymograph (bottom panel) of
1203 tdTomato-KEULE and CIT-CESA6 during a CESA exocytosis event. The kymograph shows evidence for
1204 CSC-vesicle tethering at the cell membrane (start of static phase) and successful CSC secretion as an
1205 active complex (steady movement phase, see text). (**B**) Distribution of distances between the positions of
1206 CIT-CESA6 signals at start of static phase and the nearest tdTomato-KEULE spot, as estimated by MLE
1207 PSF fitting. Data shown both for observed CIT-CESA6 locations and simulated random locations. (**C**)
1208 Differences of the observed vs expected CESA6-KEULE distance frequencies in (**B**), portraying over-
1209 and under-representation (green and red respectively). (**D**) Examples of colocalization and fitted positions
1210 for events in (**B**). (**E**) Bayesian likelihood ratios of the observed frequency of distances between 0 and 40
1211 nm given bias δ over $\delta(0.5)$. The position of the peak value indicates the most likely, or maximum a
1212 posteriori probability (MAP), value for the bias δ for the observed frequency given the expected
1213 frequency. (**F**) Bayesian analysis of the MAP(δ) for each distance bin, MAP(δ) = 0.5 indicates no
1214 difference from expected. Error bars are 95% confidence intervals expressed as the highest posterior
1215 density (HPD, the shortest interval containing 95% of the probability density). (**G**) CESA6 delivery rates
1216 in wild type and *keule* mutant cells. Data acquired from 8 cells on 8 seedlings. (Scale bars = 1μm).

1217 **Figure 3**

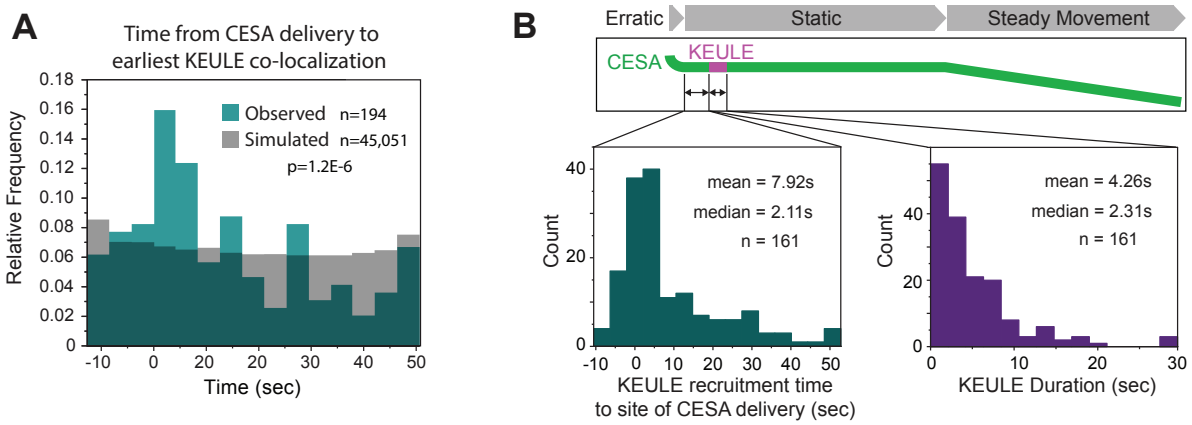

1218

1219 **Fig. 3. KEULE cluster appearance is temporally associated with CSC appearance at the plasma**
1220 **membrane.** (**A**) Comparison of the waiting time distribution from CIT-CESA6 signal stabilization until
1221 the detection of the nearest tdTomato-KEULE cluster in observed and simulated data. (**B**) KEULE
1222 dynamics in the context of CSC secretion. Histograms of waiting times (left pane) and lifetimes of
1223 tdTomato-KEULE clusters co-localized with CIT-CESA6 delivery events (right panel (**B**)).

1224 **Figure 4**

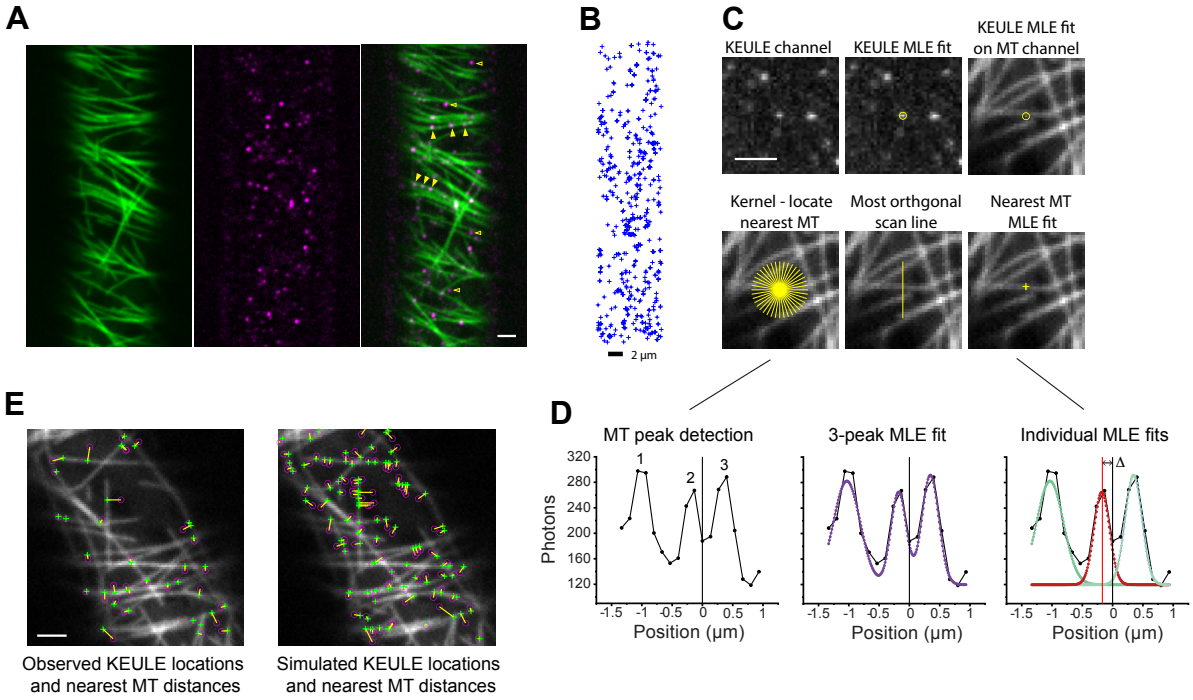

1225
1226 **Fig. 4. Microtubule dependent distribution of exocytosis events.** (**A**) Images of GFP-TUA5 and
1227 tdTomato-KEULE signal in epidermal cells. Arrowheads indicate examples of apparent co-localization of
1228 signal. (**B**) Spatial patterning of tdTomato-KEULE clusters over the range of 36.8 seconds. Crosses show
1229 positions of MLEwG fits. (**C**) Steps in the routine employed to calculation the distance from a KEULE
1230 cluster to the center of the nearest microtubule distance. (**D**) Steps in quasi-1-dimensional MLEwG fitting
1231 of microtubule signal along the most-orthogonal scan line of a rotating filter. (**E**) Overlay of a
1232 microtubule channel image and pairs of markers for MLE fit locations of KEULE clusters and the center
1233 of the nearest microtubule in observed data (left) and for simulated random KEULE locations (right).
1234 KEULE cluster detects from -5 to + 5 frames from the microtubule image are shown. Scale bars are 2 µm.

1235 **Figure 5**

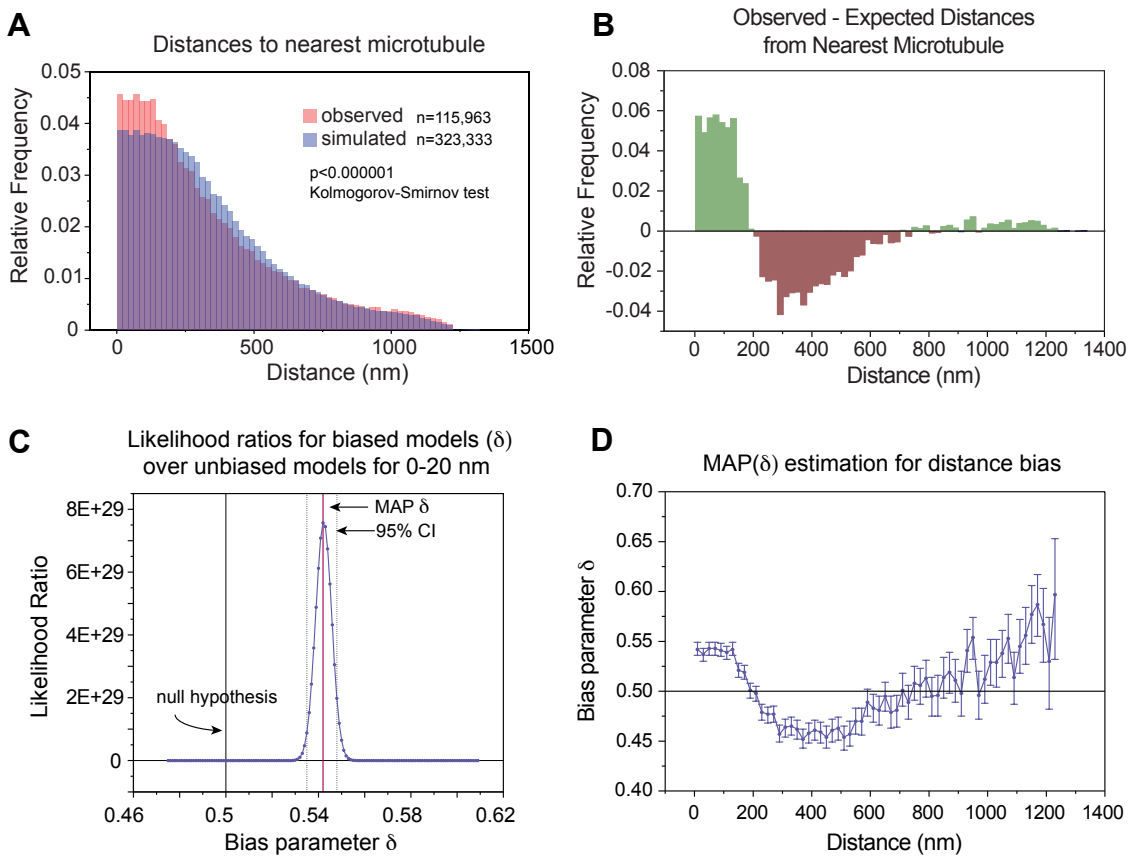

1236

1237 **Fig. 5. Bayesian analysis of microtubule bias for exocytosis events.** (**A**) Comparison of the
1238 distributions of KEULE-nearest microtubule distances for observed and simulated data. 8-12 cells (**B**)
1239 Differences of the observed vs expected KEULE-microtubule distance frequencies shown in (**A**),
1240 portraying the pattern of over- and under-representation (green and red respectively). (**C**) Bayesian
1241 likelihood ratios of the observed frequency of KEULE-microtubule distances between 0 and 20 nm given
1242 bias δ over δ(0.5). (**D**) Bayesian analysis of the MAP(δ) of each distance bin. Data acquired from 14 cells
1243 in 14 seedlings. Error bars are 95% confidence intervals expressed as HPD.

1244 **Figure 6**

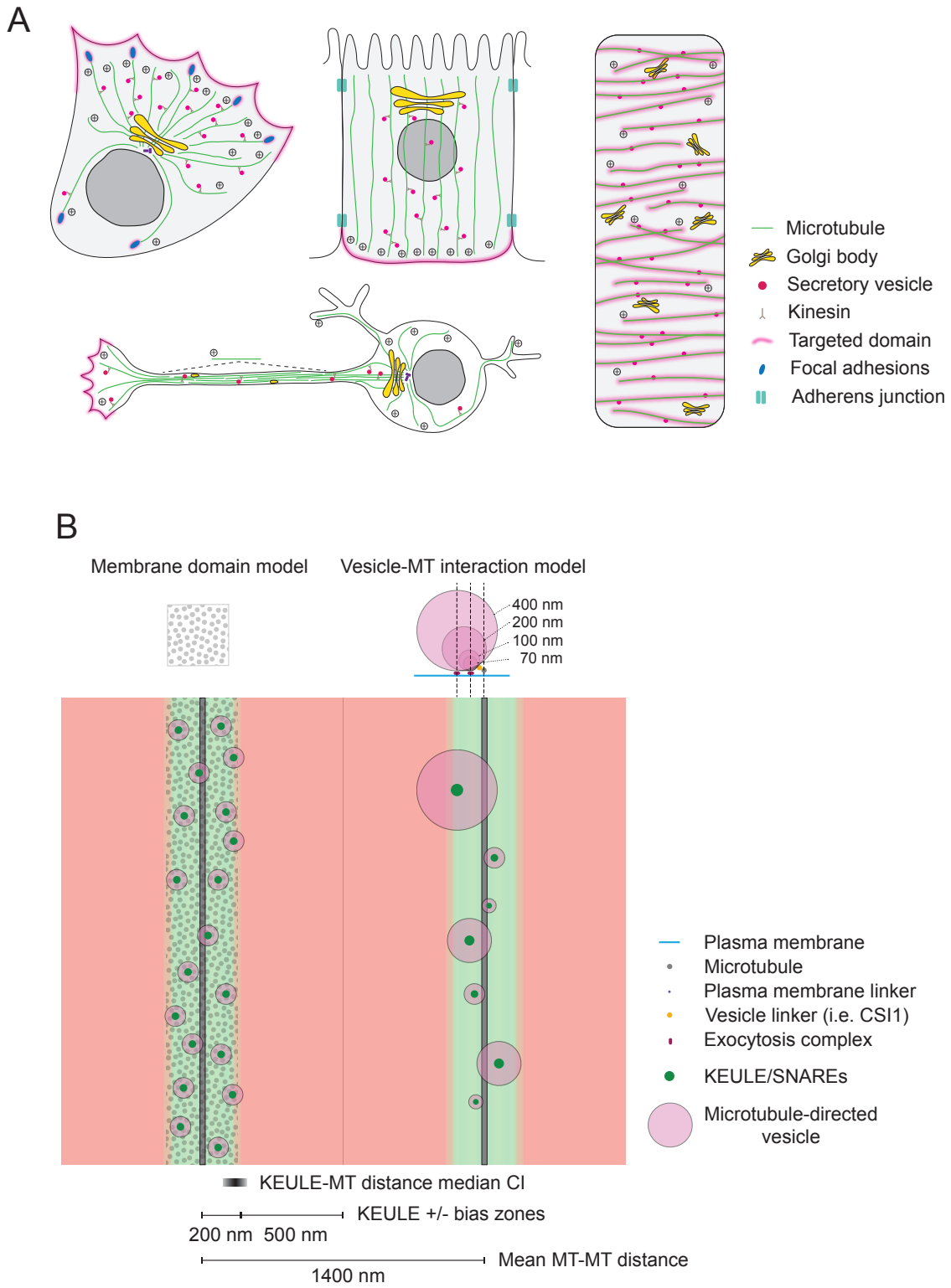

1245

1246 **Fig. 6. Patterning of secretion by microtubule arrays. (A)** Schematic diagrams of
1247 microtubule-directed patterning of secretion. The three cells on the left show targeting of
1248 secretion by motor-driven transport of secretory vesicles along polarized microtubule tracks[3] .
1249 The positioning of microtubule plus ends determines the location of cargo delivery. Clockwise
1250 from upper left: migrating fibroblast, epithelial cell, neuronal cell. By contrast, the diagram at far
1251 right shows an epidermal cell in the plant axis, where a 2-D array of microtubules at the cell
1252 cortex acts as an template that directs secretion in a complex but ordered pattern. The
1253 organization of the array as a whole defines this pattern. **(B)** Models for spatial patterning of
1254 secretion by cortical microtubule arrays in plant cells. All structures are abstracted but depicted
1255 at approximate scale. Microtubules (grey) are shown spaced at the mean spacing that has been
1256 measured in the cortical arrays of growing cells in the hypocotyl epidermis of dark grown
1257 *Arabidopsis* seedings. The red to green color between microtubules is a red-green heat map
1258 scaled from the observed over-representation and under-representation of KEULE clusters
1259 compared to that expected from a null hypothesis of a random distribution (as depicted in Fig.
1260 5B). The two sides of the diagram depict two alternative models to explain the measured spatial
1261 dimensions of the domains enriched in secretion. On the right is model where the extent of
1262 enriched domain is determined by secretory vesicle size and direct interaction of these vesicles
1263 with cortical microtubules. Secretory vesicles are depicted in a variety of sizes over a range that
1264 has been observed by SEM studies to carry cell wall secretory cargos. The diagram at the upper
1265 right relates the dimensions of these vesicles to roughly estimated locations for associated
1266 exocytotic machineries at the plasma membrane if the vesicles are targeted by direct association
1267 with microtubules by linking proteins such as CSI1. On the left, microtubules establish a
1268 membrane domain where proteins needed for vesicle capture are concentrated or secretion are
1269 concentrated. These models are not mutually exclusive. The grey scale bar at lower left depicts
1270 the mean 95% confidence interval for the measured distances of KEULE clusters to microtubule
1271 centers.